Title

Estimation of Regional Left Ventricular Function Based on Texture Analysis of Computed Tomography Images

Author

Manohar, Ashish

Publication Date

2017

UNIVERSITY OF CALIFORNIA, SAN DIEGO

Estimation of Regional Left Ventricular Function Based on Texture Analysis of Computed Tomography Images

A Thesis submitted in partial satisfaction of the requirements for the degree
Master of Science

in

Engineering Sciences (Mechanical Engineering)

by

Ashish Manohar

Committee in charge:

Professor Juan Carlos del Alamo, Chair
Professor Juan C. Lasheras
Professor Elliot R. McVeigh

2017

The Thesis of Ashish Manohar is approved and it is acceptable in quality and form for publication on microfilm and electronically:

Chair

University of California, San Diego

2017

DEDICATION

I dedicate this thesis to my Mum and Dad, for their unconditional love and support I've received throughout and for giving me this wonderful opportunity to learn and further pursue my interests.

TABLE OF CONTENTS

LIST OF FIGURES

LIST OF TABLES

ACKNOWLEDGEMENTS

First and foremost, I would like to thank my advisor, Professor Juan Carlos del Alamo, for playing a pivotal role in ensuring that my masters program was an enjoyable learning experience. I am very honored to have had the privilege of working with him. His technical and personal guidance has gone a long way in making me the better person and engineer that I am today. I am also thankful to Professor Juan C. Lasheras for agreeing to be on thesis defense committee and for his constant encouragement and support especially during the research group meetings.

I would like to thank Professor Elliot R. McVeigh for providing the CT scan data and for his time in holding helpful discussions to better optimize the tool. He has also been instrumental in giving me the confidence and encouragement to succeed.

Finally, I would like to thank my colleagues in the del Alamo lab and at UCSD. A special thanks must be made to Lorenzo Rossini for constant mentorship and getting me started with medical images. I would also like to thank Shun Zhang, Ernesto Criada-Hidalgo, and Ricardo Serrano for the helpful discussions in brainstorming issues I experienced along the way.

ABSTRACT OF THE THESIS

Estimation of Regional Left Ventricular Function Based on Texture Analysis of Computed Tomography Images

by

Ashish Manohar

Master of Science in Engineering Sciences (Mechanical Engineering)

University of California, San Diego, 2017

Professor Juan Carlos del Alamo, Chair

Assessing regional cardiac function has many diagnostic implications in the treatment of various cardiac diseases such as myocardial ischemia, cardiac dyssynchrony, etc. Unfortunately, there is no accepted gold standard for the quantitative measurement of regional cardiac function. Current methods to assess regional cardiac function primarily rely on the subjective visual analysis of cardiac images.

The method described in this thesis processes high resolution cardiothoracic CT scans to segment out and characterize the left ventricular endocardium. We hypothesize that the fractal dimension is an effective parameter to characterize and quantify the regional roughness/structure of the endocardium, which changes across the cardiac cycle.

The method was tested on 10 normal cases and on one case with heart failure. All 10 normal cases showed a consistent and uniform decrease in the fractal dimension values from end diastole to end systole whereas the heart failure case showed no considerable change, differing by 3 standard deviations from the normal cohort. The method was consistent in distinguishing normal from abnormal for all possible sizes of the local neighborhood, but showing variation in the absolute values of the fractal characterization.

Within a definite range, the method was not significantly sensitive (< 1% variation) to the initial threshold values input by the user. A study with three independent volunteers showed that the user was most likely to select a threshold value within this insensitive range.

The method developed is non-invasive, simple to use with minimum operator involvement, and computationally inexpensive.

SUMMARY

According to the World Health Organization's fact sheet, cardiovascular diseases (CVDs) are the leading cause of death globally. It has been reported that an estimated 17.7 million people died from CVDs in 2015 across the world. This estimate accounts for almost 31% of the total deaths that occurred in the world that year [1]. Management of cardiac health and timely diagnosis of cardiac diseases can reduce the number of fatalities per year.

As per the same fact sheet published by the WHO, 7.4 million of the 17.5 million deaths due to CVDs were a result of coronary heart disease, making it the primary cause of death from CVDs. Coronary heart disease is a disorder which is caused due to a disruption in the supply of blood through the coronary arteries to the heart muscle. Even a minor disruption in the supply of blood to a region of the heart muscle could potentially affect the contractility of that region, giving rise to other disorders such as shortness of breath, chest pain, etc. [2]. This has given rise to lot of interest in developing methods and tools to assess regional cardiac function. Although quantitative parameters such as ejection fraction (EF), ventricular mass, and ventricular volume shed light on cardiac performance as a whole, they do not give information on the local contractility of different regions of the heart muscle. These parameters have also been shown to be very sensitive to end diastolic volume (EDV) and end systolic pressure (ESP) [3,4].

Imaging modalities such as echocardiography, magnetic resonance imaging (MRI), and computed tomorgraphy (CT) are frequently used to diagnose and assess regional cardiac function. These methods often depend on the skill set of the operator

and the interpretation of the data maybe subjective [5]. Due to rapid advances in the temporal resolution of CT technology and due to its inherent superior spatial resolution and small acquisition times, CT is becoming an important imaging modality. It has been shown by Wu et. al. [6] that CT agrees well with MRI, which is considered the current reference cardiac imaging modality. With the advancement in cardiac imaging modalities, techniques can be developed that directly quantify regional cardiac contractility through surface characterization of the cardiac wall.

The superior spatial resolution of CT clearly delineates the structure and boundary of the endocardium (the innermost layer of the cardiac wall) as well as highlights the trabeculae and papillary muscles, which can be used as fiducial markers [7]. The trabeculae and papillary muscles of the endocardial wall behave in a similar fashion to the bellows of an accordion. They open out as the heart expands towards end diastole (like the bellows when the accordion is stretched), revealing a highly irregular structure and get compressed and smooth out (like the bellows when the accordion is compressed) as the heart squeezes towards end systole. We hypothesize that the quantification of the change in structural complexity of the trabeculae as a function of the cardiac cycle can provide information on the regional contractility.

The fractal dimension is an effective metric to measure to the complexity or structure of an object. The fractal dimension is a parameter derived from fractal theory, which describes the degree of irregularity of a surface. Fractals do not have a true definition; they can be thought of as extremely complex structures which cannot be described by our conventional knowledge of geometry and dimension. One of the most famous fractals is the Koch Curve. It is neither a line, nor a surface and hence cannot be categorized as either 1-dimensional (1D) nor 2-dimensional (2D).

The method developed processes cardiothoracic CT scans of patients to segment out the left ventricular endocardium and characterizes it with a map of its local fractal dimension values. The local fractal dimension is calculated for regions of the endocardium defined by a neighborhood cube of size 64 voxels. The map describes the regional complexity in the structure of the endocardium and tracking changes in this parameter across the cardiac cycle can provide information on the regional contractility or health of the endocardium.

There is a window of threshold values for each CT scan within which the algorithm is not significantly sensitive. The fractal dimension varies less than 1% between threshold values in tis range. The algorithm also distinguished between the normal cohort and the heart failure case consistently for all possible neighborhood sizes by three standard deviations. However, there was a difference in the absolute values of the regional characterization of the endocardium due to the different length scales at which the fractal dimension was computed.

The method developed was simple, quick, easy to use, requires minimal operator involvement, and requires minimal exposure of the patient to ionizing radiations. We hypothesize that the method can aid physicians in the diagnosis of cardiac disorders such as heart failure, myocardial ischemia, and myocardial dyssynchrony.

References

[1] World Health Organization. (2017). Cardiovascular diseases (CVDs) Fact sheet. Retrieved from http:// http://www.who.int/mediacentre/factsheets/fs317/en.

[2] Ross, J. Jr. (1999). Regional Myocardial Microvascular Dysfunction. Does the Alternate Cascade Represent Ischemia? *Cardiologia (Rome, Italy), 44*(9), 797-799.

[3] Quiñones, M. A., Gaasch, W. H., & Alexander, J. K. (1976). Influence of acute changes in preload, afterload, contractile state and heart rate on ejection and isovolumic indices of myocardial contractility in man. *Circulation*, *53*(2), 293-302.

[4] Thomas, J. D., & Popović, Z. B. (2006). Assessment of left ventricular function by cardiac ultrasound. *Journal of the American College of Cardiology*, *48*(10), 2012-2025.

[5] Hung, J., Francois, C., Nelson, N. A., Young, A., Cowan, B. R., Jerecic, R., & Carr, J. (2009). Cardiac image modeling tool for quantitative analysis of global and regional cardiac wall motion. *Investigative radiology*, *44*(5), 271-278.

[6] Wu, Y. W., Tadamura, E., Yamamuro, M., Kanao, S., Okayama, S., Ozasa, N., ... & Togashi, K. (2008). Estimation of global and regional cardiac function using 64-slice computed tomography: a comparison study with echocardiography, gated-SPECT and cardiovascular magnetic resonance. *International journal of cardiology*, *128*(1), 69-76.

[7] Pourmorteza, A., Schuleri, K. H., Herzka, D. A., Lardo, A. C., & McVeigh, E. R. (2012). A New Method for Cardiac Computed Tomography Regional Function AssessmentClinical Perspective. *Circulation: Cardiovascular Imaging*, *5*(2), 243-250.

Chapter 1

INTRODUCTION

This chapter gives a brief introduction to the anatomy of the human heart and the circulatory system. It also provides a summary of the current methods in use to measure and assess regional cardiac function and their advantages and disadvantages. Lastly, the chapter deals with the rationale behind the method described in this thesis as well as a brief theoretical overview of fractal geometry.

1.1 Anatomy of the Human Heart

The heart is an organ located close to the center of the thoracic cavity. It is located between the right and left lungs towards the left of the breastbone as shown in Figure 1.1. It is enclosed by a thin, inelastic fibrous bag called the pericardium which connects the heart to the sternum. It is the primary organ of the circulatory system and responsible for pumping blood throughout the body.

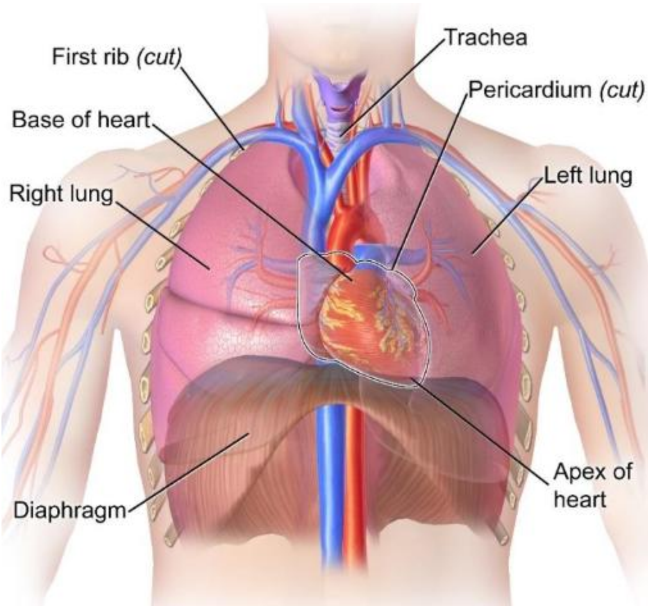

Figure 1.1. Schematic diagram of the human thoracic cavity showing the position of the heart relative to other organs in the body. [1]

The circulation of blood in the body is divided into two main systems; pulmonary and systemic circulation. Pulmonary circulation is the movement of blood between the heart and the lungs and is responsible for the exchange of gases and oxygenation of the blood in the lungs. A graphical description of pulmonary circulation is shown in Figure 1. 2.

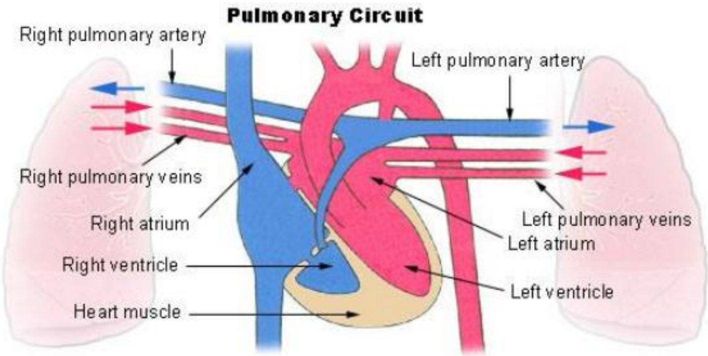

Figure 1.2. Schematic diagram of pulmonary circulation. [2]

Systemic circulation is the transportation of blood between the heart and all other parts of the body. Figure 1.3 is a schematic representation of systemic circulation.

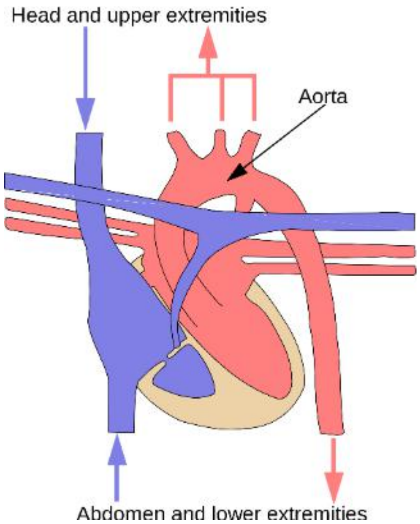

Figure 1.3. Schematic diagram of systemic circulation. [3]

The heart has 4 chambers; the left atrium, the right atrium, the left ventricle, and the right ventricle. The right atrium receives deoxygenated blood from the superior and inferior vena cavas and empties into the right ventricle through the tricuspid valve. The left atrium receives oxygenated blood from the pulmonary veins and empties into the left ventricle through the mitral valve. The ventricles are the pumping chambers, with the left ventricle pumping blood, through the aorta, to different parts of the body (systemic circulation) and the right ventricle pumping blood, through the pulmonary artery, to the lungs (pulmonary circulation). Figure 1.4 shows the general structure of the human heart.

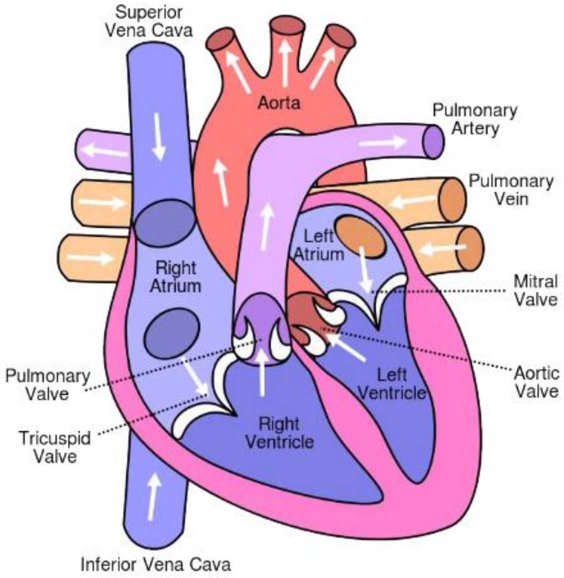

Figure 1.4. Anatomy of the human heart. [4]

The heart wall consists of three layers: the epicardium, the myocardium, and the endocardium, as shown in Figure 1.5. These layers are surrounded by the pericardium and the pericardial fluid. The innermost layer, called the endocardium, is made up of simple squamous epithelial tissue. The middle layer, called the myocardium, forms the bulk of the cardiac wall and is made up of special type of muscle cells called cardiac muscle cells or cardiomyocytes and is connected to the endocardium through a layer of connective tissue. The outer layer, called the epicardium, is made up of two layers of mesothelium in the form of a serous membrane [5].

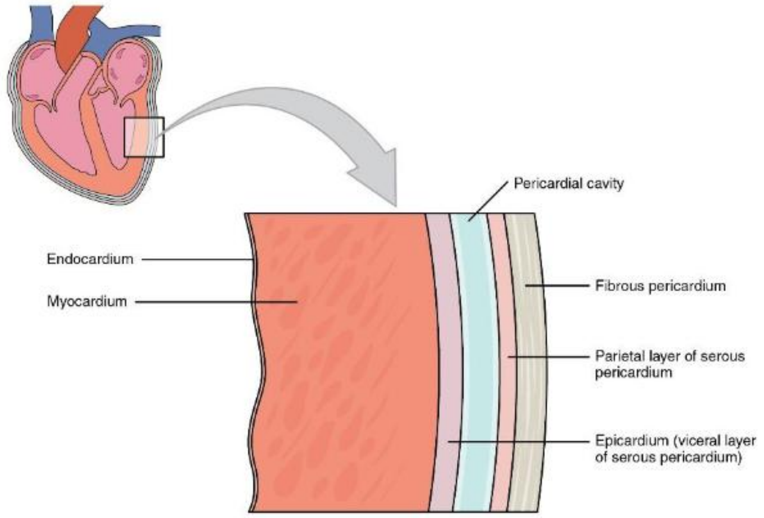

Figure 1.5. Schematic representation of the human left ventricular wall. [5]

In this thesis, we will focus our attention on the left ventricle as it is the chamber responsible for systemic circulation and its proper health and functioning has important implications on cardiac health. The left ventricle is also much thicker as compared to the right, and this is due to the larger forces it needs to withstand for systemic circulation [5].

The heart is supplied with blood by the left and right coronary arteries and their corresponding branches. The coronaries branch out from the aorta just above the mitral valve opening. It is the disruption of blood flow in these coronary arteries which account for the 7.4 million deaths globally as reported by the WHO.

1.2 Assessment of Cardiac Function

Assessing regional cardiac function has important implications in the diagnosis and clinical management of cardiac disorders. With advances in cardiac imaging modalities, the non-invasive assessment of regional cardiac function has become more accurate over time. Superior spatial and temporal resolutions allow us to measure wall thickening, regional strain, LV ejection fraction (EF), and LV mass. Currently, there are many modalities that are routinely used to assess regional cardiac function.

Echocardiography is a favored imaging modality to evaluate cardiac health. Its ease of use, low cost and real time imaging are some of the key advantages [6]. However, the technique is 2D (recent developments in 3D technology have emerged) and applies geometric assumptions to the image. This can have a negative impact on the accuracy of assessing the EF. Also, its spatial resolution is low and hence cannot perfectly delineate the endocardial and epicardial borders [7].

Cardiac magnetic resonance imaging (cMRI) serves as the current reference standard in assessment of cardiac function. [8,9]. It produces 3D images and has good spatial and excellent temporal resolution. However, the imaging is slow and requires breath holding and multiple passes. The spatial resolution lacks in its ability to completely delineate endocardial structures such as the trabeculae, leading to overestimation and underestimation of ventricular volume at diastole and systole respectively [10]. Also, cMRI cannot be performed on patients implanted with pacemakers and other metallic devices and this is a severe limitation with the increasing number of patients using such devices.

With the advent of 256 slice scanners, improved temporal resolution, and quicker scanning times, CT technology is emerging as a strong contender for assessing cardiac function [6]. CT also provides the added benefit of combining a high-resolution angiogram study together with a study to assess global and regional cardiac function [11]. Previous studies have also shown good agreement of global and regional cardiac function assessment between CT and MRI [12-16]. With its excellent spatial resolution, CT technology can clearly delineate the interface between the endocardium and the blood pool, which makes segmentation easy. Another advantage of CT over other imaging modalities is that it is less operator dependent. The drawback of CT technology, however, is the exposure of the patient to strong ionizing radiations.

While global cardiac function has been routinely estimated using EF as a parameter [9, 17], current methods for assessing regional cardiac function rely primarily on visual inspection [9, 18-19]. EF and other volumetric indices are very sensitive to pre-load (EDV) and after-load (ESP), reducing their efficacy of quantifying regional cardiac function. [20-21].

Regional cardiac function can be determined through a qualitative description of regional wall motion [6,9,19,22], or by using a quantitative approach to track myocardial deformations across the cardiac cycle [23]. One parameter describing myocardial deformation is wall thickening. It has been shown by Lieberman et al. [24] that a quantitative measurement of myocardial thickening is more accurate than a visual analysis of wall motion. Analysis of wall thickening through 2D slices, depicts changes only in the radial direction, failing to take into consideration the thickening occurring in the circumferential and longitudinal directions, hence not providing a complete and true measurement [25-26]. Another technique of quantifying regional cardiac function is through the measurement of regional strain. This method provides a sufficient and accurate model and accounts for changes occurring in the wall across the cardiac cycle in all the three principal directions [27-29]. However, the method is involved requiring complex image processing and registration algorithms.

1.3 Rationale

The endocardium of the human left ventricle is lined with muscular ridges called trabeculae carneae and papillary muscles. While the papillary muscles are used to control the mitral and aortic valves, the trabeculae are considered to have a passive role [30]. However, Moore and Dasi showed in their work that the structure of the trabeculae change considerably across the cardiac cycle [31]. At end diastole, the trabeculae open out and present a rough endocardial surface while at end systole, the trabeculae squeeze in and smooth out, in a manner similar to the opening and closing of the bellows of an accordion.

The availability of wide-range detector CT technology has made the acquisition of high resolution images of the LV endocardium possible, which clearly delineate the fine anatomical structures and capture the full complexity of the surface structure of the endocardial wall. We hypothesize that through these high resolution images, the regional roughness or structure of the endocardium can be characterized. We hypothesize that the fractal dimension is an effective parameter to quantify the regional roughness and by tracking changes in the fractal values across the cardiac cycle, information about the regional health and contractility of the left ventricle can be obtained.

1.4 Fractals

Many a time in nature, we encounter structures that are compactly packed, exhibiting a convoluted or “rough” topology. Broccoli is a classic example that can be used to illustrate this point. The surface of the broccoli is so complex and convoluted that even though it occupies a finite volume, it’s surface area is extremely large. Intuitively, the broccoli surface is considered to be 3-dimensional, although it does not entirely occupy a full 3-dimensional volume. The theoretical dimension of broccoli is estimated to be about 2.7 [32], which gives us information on its structure (too complex to be 2-D while not being fully 3-D). Other common examples which can be described using fractal theory are fluid turbulence, topology of clouds and coastlines, etc.

There is no one comprehensive definition of a fractal. Benoit Mandelbrot, who first coined the term ‘fractal’, defined a fractal as an irregular set whose Hausdorff dimension exceeded its topological dimension. This definition does not hold good for certain cases and is therefore not a comprehensive definition. To better understand fractal theory, let us examine a few classical fractal sets:

a) <u>Von Koch curve:</u> The von Koch curve is generated by dividing every line segment into 3 equal parts and replacing the middle part with two lines, each of length equal to the length of the replaced part and arranged in a manner to form the sides of an equilateral triangle as shown in Figure 1.6 below.

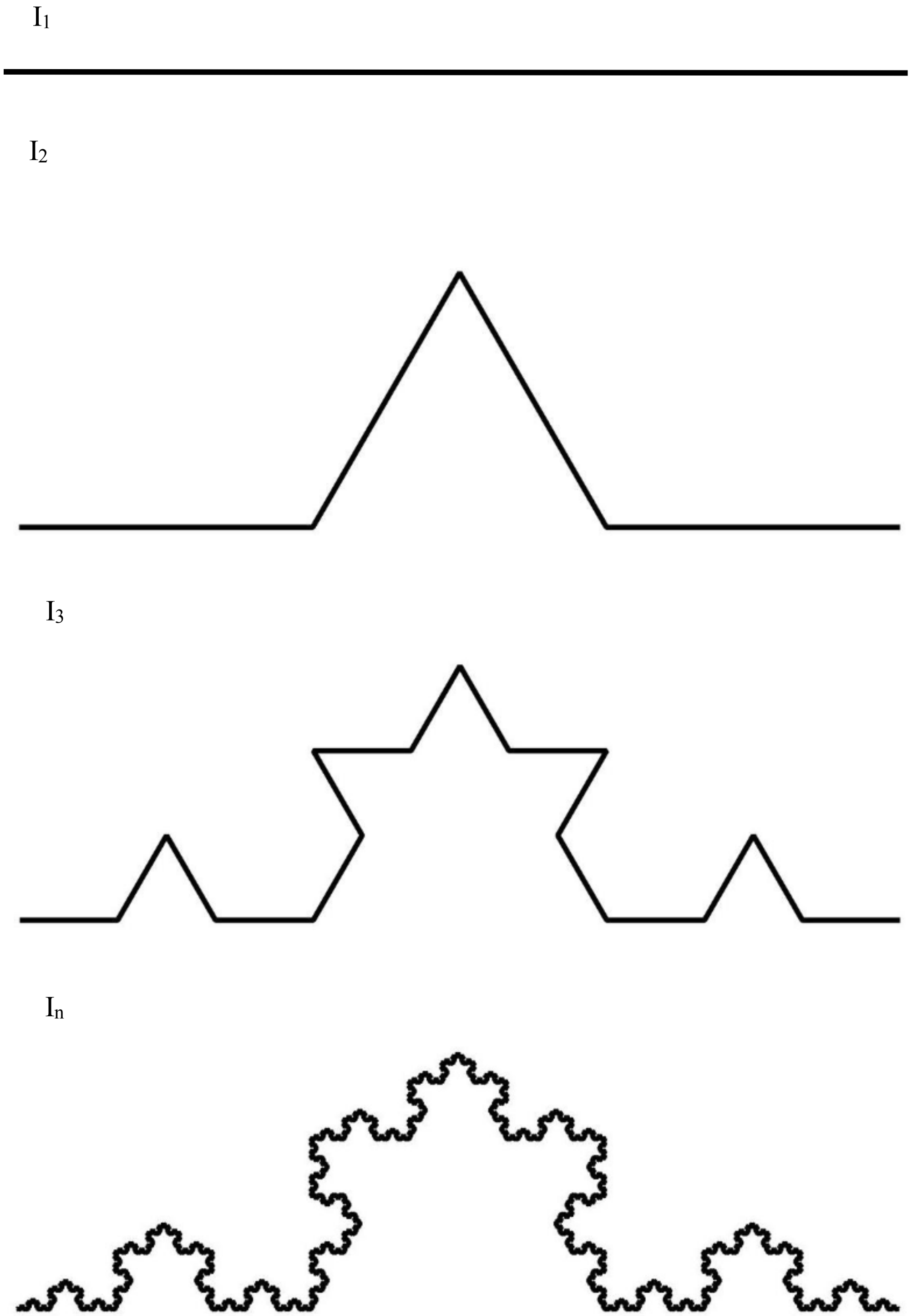

Figure 1.6. Different iterations of the generation of the von Koch curve.

b) Sierpinski triangle: The Sierpinski triangle is an equilateral triangle, which at each iteration is divided into 4 equilateral triangles, 3 at the 3 respective corners of the parent triangle and the 4th one being an inverted equilateral triangle at the center. The center triangle is removed at each iteration, leaving a void in the middle as shown in Figure 1.7 below.

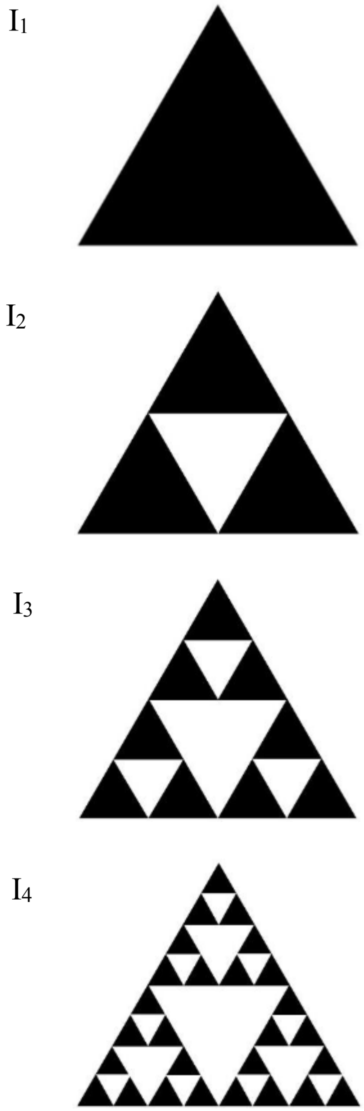

Figure 1.7. Different iterations of the generation of the Sierpinski Triangle

Examining the above examples, two main characteristics of fractal sets can be described:

- They have an extremely fine structure. Even to infinite magnification, there is always new information revealed by the set.
- These sets exhibit a self-repeating nature. Magnification of a certain area of the set, reveals patterns that resemble the original set.

These sets cannot truly be described using our conventional knowledge of Euclidean geometry. Concepts such as length and area, when used to describe these sets, do not provide us with physically relevant information. This point will be elaborated on later in this chapter.

1.4.1 Natural & Deterministic Fractals

A distinction must be made between natural and deterministic fractals. Prior to the advent of fractal theory, nature was thought to be a form of noisy Euclidean geometry [33]. Although fractals generated through mathematical operations (deterministic fractals) are truly self-similar and have an infinitely fine structure, fractals occurring in nature are not truly self-similar but show statistical self-similarity. Beyond a certain level of magnification, we will start to observe atoms and molecules which aren't representative of the overall original structure. A classical example used to illustrate this point is the human brain. At very high magnification levels, we will begin to observe the cellular structure of the brain. However, between this upper and lower limit of magnification, natural fractals exhibit some form of self-similarity; a branch of a tree resembles the entire tree, the sub-branches resemble the parent branch and so on until the magnification scale breaks down and no further detail is seen.

1.4.2 Euclidean & Topological Dimension

To better understand the term dimension, consider a line and two systems by which its dimension can be characterized. The Euclidean dimension characterizes objects according to the number of independent parameters required to fully define every point on the object. On the other hand, the Topological dimension characterizes objects solely based on their topology and structure. Figure 1.8 shows a line in 3-dimensional Euclidean space. For this particular line, the Euclidean dimension is 3 because any point on the line is defined by the x,y, and z coordinates. However, the topological dimension of the line remains 1 as it is independent of the orientation of the line.

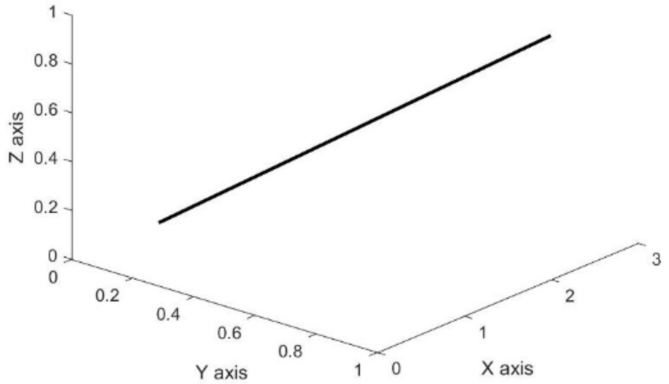

Figure 1.8. A line in 3-dimensional Euclidean space

Therefore, the topological dimension of a point, line, plane, and volume is always 0, 1, 2 and 3 respectively. Figure 1.9 shows a fractal that is generated through an iterative procedure which resembles the structure of cauliflower. For this figure, neither the Euclidean nor the Topological dimension will provide a good structural description due to the irregularity of the surface. Therefore, to better characterize the topology and space filling characteristics of such irregular figures, the *fractal dimension* is used. The name was used to express a form of "fractured dimensions", introduced by Benoit Mandelbrot in his paper on self-similarity [35].

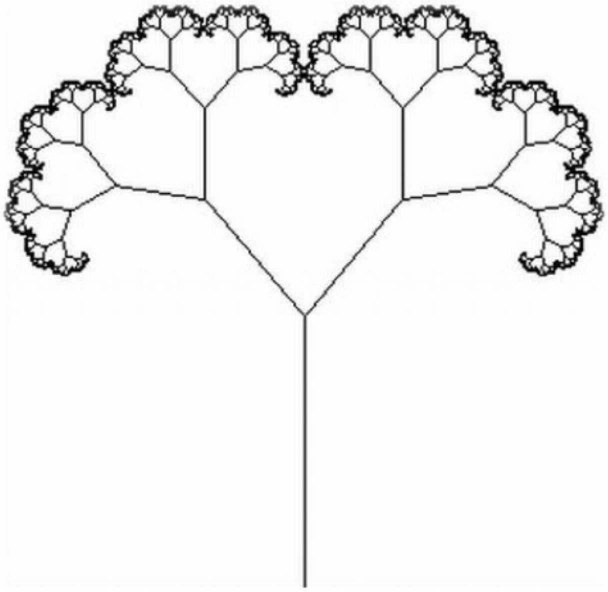

Figure 1.9. A cauliflower generated through an iterative process. [34]

1.4.3 Fractal Dimension

The von Koch curve is an ideal example to understand the concept of "fractional" or "fractured" dimension. In Figure 1.6, it is seen that with every iteration, the line segment is divided into 3 parts and as a result of this division, 4 new parts are created. In other words, for a reduction scale of (1/3), 4 new parts are created. Thus,

$$\left(\frac{1}{3}\right)^{d} = 4,$$

where 'd' is the fractal dimension. On solving for d, we get $d = \frac{\log(4)}{\log(3)}$ = 1.2619. Regular geometric figures scale in a similar manner, the only difference being that they scale as a whole number and not as a fraction. For example, consider a square. On scaling the square down by half, i.e. dividing every line of the square into half, we obtain 4 squares. Similarly, if we scale it down by one-third, then we get 9 squares as shown in Figure 1.10. Therefore, representing it mathematically,

$$d = \frac{\log(4)}{\log(2)} = \frac{\log(9)}{\log(3)} = 2.$$

This value of 2 gives us the 2-dimensional characteristics of a square. The same procedure can be repeated with a cube and the value of d will be 3 in that case.

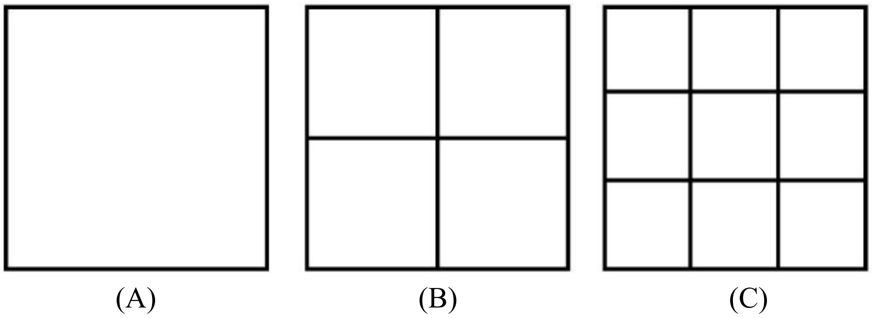
(A) (B) (C)

Figure 1.10. Scaling laws for a square. (A)Full square – 1 unit. (B) Dividing by half – 4 units. (C) Dividing by one-third – 9 units.

The Sierpinski triangle can be used to truly understand the complexity or irregularity of the fractals and the need for a fractional dimension. From Figure 1.7, it is observed that the length of the Sierpinski triangle tends to infinity while its area tends to 0. To prove this, let k be the number of iterations in the generation of the Sierpinski set. The length is given by the relation:

$$Length \ = 3 + \left(\frac{3}{2}\right)^{k},$$

where the length of the side of the parent triangle is taken as unity. Therefore, as k → infinity, length → infinity. Similarly, the area is given by the relation:

$$Area = \ 3^{k}.(2^{-k})^{2}.\frac{\sqrt{3}}{4}$$

As k → infinity, the area → 0. Thus, geometrical concepts such as length and area do not provide physically relevant information of the structure of these irregular figures. Length is used as a parameter to measure sets of dimension 1 and area is used to measure sets of dimension 2. But the Sierpinski triangle has an infinite length and zero area, and this phenomenon was first justified by Hausdorff in 1919 when he proposed that the dimension of a set should be allowed to be a fraction [36].

References

[1] Blausen, Bruce (Artist). (2013) *Location of Heart in Thoracic Cavity* [Digital Image]. Retrieved from Wikimedia Commons website: https://commons.wikimedia.org/wiki/File:Blausen_0458_Heart_ThoracicCavity.png

[2] United States Government. (2006) *Pulmonary Circuit* [Digital Image]. Retrieved from Wikimedia Commons website: https://commons.wikimedia.org/wiki/File:Illu_pulmonary_circuit.jpg

[3] Surachit (Artist). (2007) *Systemic Circulation* [Digital Image]. Retrieved from Wikimedia Commons website: https://commons.wikimedia.org/wiki/File:Illu_systemic_circuit.svg

[4] Wapcaplet (Artist). (2006) *Diagram of the Human Heart* [Digital Image]. Retrieved from Wikimedia Commons website: https://commons.wikimedia.org/wiki/File:Diagram_of_the_human_heart_(cropped).svg

[5] Betts, J. Gordon (2013). *Anatomy & Physiology*. Houston, TX: OpenStax College.

[6] Hung, J., Francois, C., Nelson, N. A., Young, A., Cowan, B. R., Jerecic, R., & Carr, J. (2009). Cardiac image modeling tool for quantitative analysis of global and regional cardiac wall motion. *Investigative radiology*, *44*(5), 271-278.

[7] Kühl, H. P., Spuentrup, E., Wall, A., Franke, A., Schröder, J., Heussen, N., ... & Buecker, A. (2004). Assessment of Myocardial Function with Interactive Non–Breath-hold Real-time MR Imaging: Comparison with Echocardiography and Breath-hold Cine MR Imaging 1. *Radiology*, *231*(1), 198-207.

[8] Finn, J. P., Nael, K., Deshpande, V., Ratib, O., & Laub, G. (2006). Cardiac MR imaging: State of the technology 1. *Radiology*, *241*(2), 338-354.

[9] Wu, Y. W., Tadamura, E., Yamamuro, M., Kanao, S., Okayama, S., Ozasa, N., ... & Togashi, K. (2008). Estimation of global and regional cardiac function using 64-slice computed tomography: a comparison study with echocardiography, gated-SPECT and cardiovascular magnetic resonance. *International journal of cardiology*, *128*(1), 69-76.

[10] Busch, S., Johnson, T. R. C., Wintersperger, B. J., Minaifar, N., Bhargava, A., Rist, C., ... & Nikolaou, K. (2008). Quantitative assessment of left ventricular

function with dual-source CT in comparison to cardiac magnetic resonance imaging: initial findings. *European radiology*, *18*(3), 570-575.

[11] Pourmorteza, A., Chen, M. Y., van der Pals, J., Arai, A. E., & McVeigh, E. R. (2016). Correlation of CT-based regional cardiac function (SQUEEZ) with myocardial strain calculated from tagged MRI: an experimental study. *The international journal of cardiovascular imaging*, *32*(5), 817-823.

[12] Juergens, K. U., Grude, M., Maintz, D., Fallenberg, E. M., Wichter, T., Heindel, W., & Fischbach, R. (2004). Multi–Detector Row CT of Left Ventricular Function with Dedicated Analysis Software versus MR Imaging: Initial Experience 1. *Radiology*, *230*(2), 403-410.

[13] Yamamuro, M., Tadamura, E., Kanao, S., Wu, Y. W., Tambara, K., Komeda, M., ... & Togashi, K. (2007). Coronary angiography by 64-detector row computed tomography using low dose of contrast material with saline chaser: influence of total injection volume on vessel attenuation. *Journal of computer assisted tomography*, *31*(2), 272-280.

[14] Yamamuro, M., Tadamura, E., Kubo, S., Toyoda, H., Nishina, T., Ohba, M., ... & Kita, T. (2005). Cardiac Functional Analysis with Multi–Detector Row CT and Segmental Reconstruction Algorithm: Comparison with Echocardiography, SPECT, and MR Imaging 1. *Radiology*, *234*(2), 381-390.

[15] Heuschmid, M., Rothfuss, J. K., Schroeder, S., Fenchel, M., Stauder, N., Burgstahler, C., ... & Claussen, C. D. (2006). Assessment of left ventricular myocardial function using 16-slice multidetector-row computed tomography: comparison with magnetic resonance imaging and echocardiography. *European radiology*, *16*(3), 551-559.

[16] Raman, S. V., Shah, M., McCarthy, B., Garcia, A., & Ferketich, A. K. (2006). Multi–detector row cardiac computed tomography accurately quantifies right and left ventricular size and function compared with cardiac magnetic resonance. *American heart journal*, *151*(3), 736-744.

[17] Dewey, M., Müller, M., Eddicks, S., Schnapauff, D., Teige, F., Rutsch, W., ... & Hamm, B. (2006). Evaluation of global and regional left ventricular function with 16-slice computed tomography, biplane cineventriculography, and two-dimensional transthoracic echocardiography: comparison with magnetic resonance imaging. *Journal of the American College of Cardiology*, *48*(10), 2034-2044.

[18] Earls, J. P., Ho, V. B., Foo, T. K., Castillo, E., & Flamm, S. D. (2002). Cardiac MRI: recent progress and continued challenges. *Journal of magnetic resonance imaging*, *16*(2), 111-127.

[19] Underwood, S. R., Rees, R. S., Savage, P. E., Klipstein, R. H., Firmin, D. N., Fox, K. M., ... & Longmore, D. B. (1986). Assessment of regional left ventricular function by magnetic resonance. *British heart journal*, *56*(4), 334-340.

[20] Quiñones, M. A., Gaasch, W. H., & Alexander, J. K. (1976). Influence of acute changes in preload, afterload, contractile state and heart rate on ejection and isovolumic indices of myocardial contractility in man. *Circulation*, *53*(2), 293-302.

[21] Thomas, J. D., & Popović, Z. B. (2006). Assessment of left ventricular function by cardiac ultrasound. *Journal of the American College of Cardiology*, *48*(10), 2012-2025.

[22] Hoffmann, R., von Bardeleben, S., Kasprzak, J. D., Borges, A. C., ten Cate, F., Firschke, C., ... & Greis, C. (2006). Analysis of regional left ventricular function by cineventriculography, cardiac magnetic resonance imaging, and unenhanced and contrast-enhanced echocardiography. *Journal of the American College of Cardiology*, *47*(1), 121-128.

[23] Lardo, A. C., Abraham, T. P., & Kass, D. A. (2005). Magnetic resonance imaging assessment of ventricular dyssynchrony: current and emerging concepts. *Journal of the American College of Cardiology*, *46*(12), 2223-2228.

[24] Lieberman, A. N., Weiss, J. L., Jugdutt, B. I., Becker, L. C., Bulkley, B. H., Garrison, J. G., ... & Weisfeldt, M. L. (1981). Two-dimensional echocardiography and infarct size: relationship of regional wall motion and thickening to the extent of myocardial infarction in the dog. *Circulation*, *63*(4), 739-746.

[25] Spotnitz, H. M. (2000). Macro design, structure, and mechanics of the left ventricle. *The Journal of Thoracic and Cardiovascular Surgery*, *119*(5), 1053-1077.

[26] Castillo, E., Lima, J. A., & Bluemke, D. A. (2003). Regional Myocardial Function: Advances in MR Imaging and Analysis 1. *Radiographics*, *23*(suppl_1), S127-S140.

[27] Moore, C. C., McVeigh, E. R., & Zerhouni, E. A. (2000). Quantitative tagged magnetic resonance imaging of the normal human left ventricle. *Topics in magnetic resonance imaging: TMRI*, *11*(6), 359.

[28] McVeigh, E. (1998). Regional myocardial function. *Cardiology clinics*, *16*(2), 189-206.

[29] Pourmorteza, A., Schuleri, K. H., Herzka, D. A., Lardo, A. C., & McVeigh, E. R. (2012). A New Method for Cardiac Computed Tomography Regional Function AssessmentClinical Perspective. *Circulation: Cardiovascular Imaging*, *5*(2), 243-250.

[30] Burch, G. E., Ray, C. T., & Cronvich, J. A. (1952). The George Fahr Lecture. *Circulation*, *5*(4), 504-513.

[31] Moore, B., & Dasi, L. P. (2013). Quantifying left ventricular trabeculae function–application of image- based fractal analysis. *Physiological reports*, *1*(4), e00068.

[32] Kim, S. H. (2004). Fractal structure of a white cauliflower. *arXiv preprint cond-mat/0409763*.

[33] Nilsson, E. (2007). Multifractal-based image analysis with applications in medical imaging. *Dep. Comput. Sci. Umea Univ. Umea Sweden*, 33-70.

[34] Frame, M., Mandelbrot, B., & Nial Neger. *Fractal Geometry*. Retrieved from http://classes.yale.edu/Fractals/Welcome.html

[35] Mandelbrot, B. B. (1967). How long is the coast of Britain. *Science*, *156*(3775), 636-638.

[36] Edgar, G. (2007). *Measure, topology, and fractal geometry*. Springer Science & Business Media.

Chapter 2

METHODS

This chapter describes the tools, functions, and processes that are employed to achieve the regional characterization of the left ventricular (LV) endocardium. An overview of the processes involved is shown below in the form of a process flowchart:

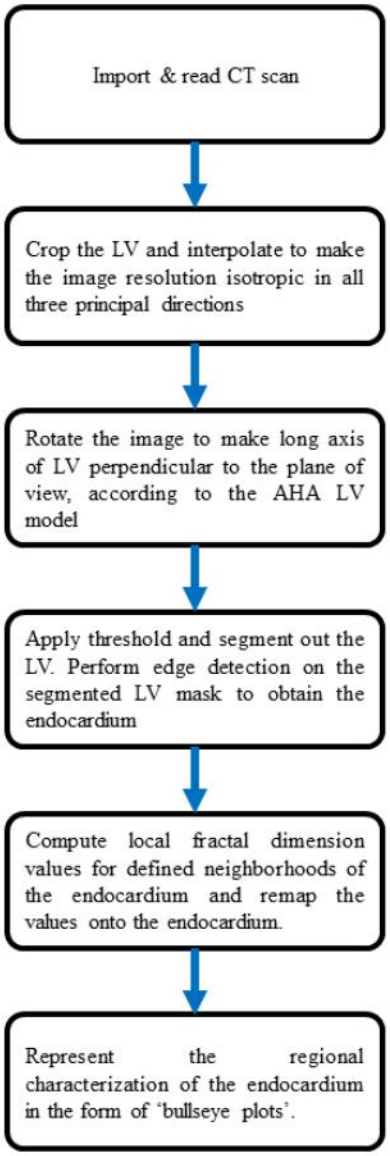

Import & read CT scan

Crop the LV and interpolate to make the image resolution isotropic in all three principal directions

Rotate the image to make long axis of LV perpendicular to the plane of view, according to the AHA LV model

Apply threshold and segment out the LV. Perform edge detection on the segmented LV mask to obtain the endocardium

Compute local fractal dimension values for defined neighborhoods of the endocardium and remap the values onto the endocardium.

Represent the regional characterization of the endocardium in the form of 'bullseye plots'.

2.1 Image Processing

All computations were performed using *Matlab R2015b* (MathWorks Inc.), unless specified otherwise. *Matlab* offers great versatility in reading and processing medical images.

2.1.1 CT Scans & DICOM Files

CT scans are generated by imaging parts of the body using X-rays from different angles and positions and reconstructing the different images acquired into a 3-dimensional volume. They provide more detailed information as compared to plain X-ray images. A typical CT scanner is shown in Figure. 2.1.

Figure 2.1. Modern CT Scanner (GE Healthcare). [1]

'Digital Imaging and Communications in Medicine' (DICOM) is the standard for storing medical images from different imaging modalities, including but not limited to CT scans, magnetic resonance imaging (MRIs), ultrasonography, etc. Each DICOM (.dcm) file stores the CT scan images as either 2-D slices or a stack-up of 2-D slices forming an entire 3-D volume.

The DICOM files are imported and read into *Matlab* through the *dicomread* function. The files, depending on the information they contain (either 2-D slices or 3-D volume), are imported in a manner so as to reconstruct a 3-D volume for every time point imaged during the CT scan. For example, if the CT scan is imaged over 20 different time points across the cardiac cycle, the DICOM files are reconstructed to form 20 different 3-D volumes representing the different phases of cardiac contraction. As this set of data has 3-dimensions for every time point, it is sometimes referred to as 4-D, time being the 4th "dimension".

2.1.2 Image Cropping & Interpolation

To minimize computation time and memory usage, a rough crop around the left ventricle is made to isolate it from the rest of the cardiothoracic CT scan. Pre and post cropping images are shown in Figure 2.2. From this point, any reference to a 3-D volume is a reference to only the 3-D data of the left ventricle.

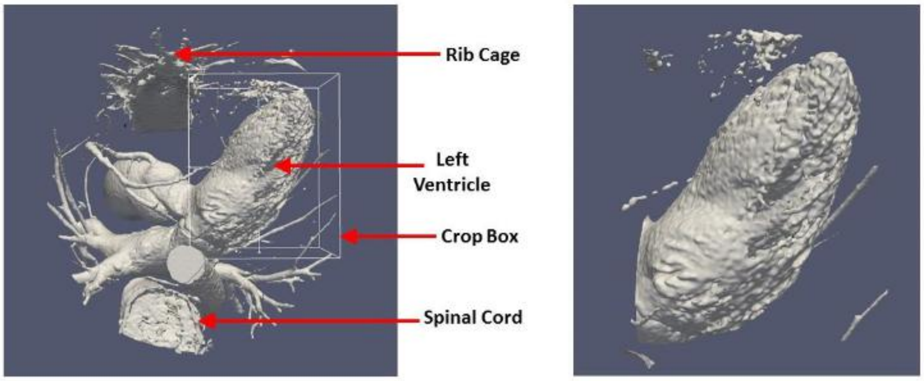

(A) (B)

Figure 2.2. Cropping of the left ventricle. (A) 3-D reconstruction of a Cardiac CT scan. (B) The left ventricle cropped out.

Depending on the model and manufacturer, each CT scanner may have different resolutions in the X,Y,and Z directions. The method introduced and described in this thesis is isotropic in nature and hence necessitates an equal pixel representation in all the three principal directions. To compensate for this inequality in resolution, a 3-D linear interpolation is performed on the image data of every time frame. For example, if the resolutions in X,Y, and Z are 0.3mm x 0.3mm x 1mm respectively, (1/0.3) times the number of initial points in Z are added to Z. Although this process of interpolating does not increase the image resolution, it does add more number of sampling points to make all three principal directions isotropic.

2.1.3 Image Rotation

The axes of the CT images are aligned with the longitudinal and transverse axes of the human body as shown in Figure 2.3. However, the left ventricle is not aligned with either one of these axes; the long axis of the left ventricle is oriented in an oblique manner in relation to each of the three principal axes.

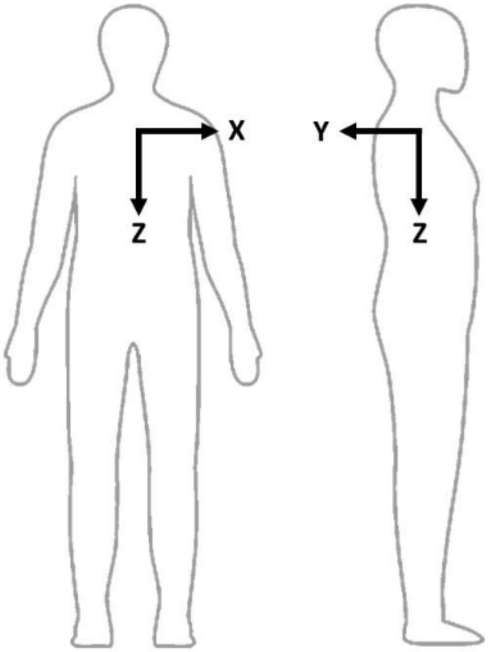

Figure 2.3. Axes orientation of the CT images in reference to the human body.

According to Heller et al., in their work published in the American Heart Association (AHA) Scientific Statement in 2002 [2], the standardized LV nomenclature and segmentation model necessitates the long axis of the LV to be perpendicular and into the plane of view. Additionally, the standard recommends that the left ventricle to be oriented in a manner so as to have the anterior side positioned at 12 o’clock, the lateral side positioned at 3 o’clock, the inferior side positioned at 6 o’clock, and the septal side positioned at 9 o’clock as shown in Figure 2.4.

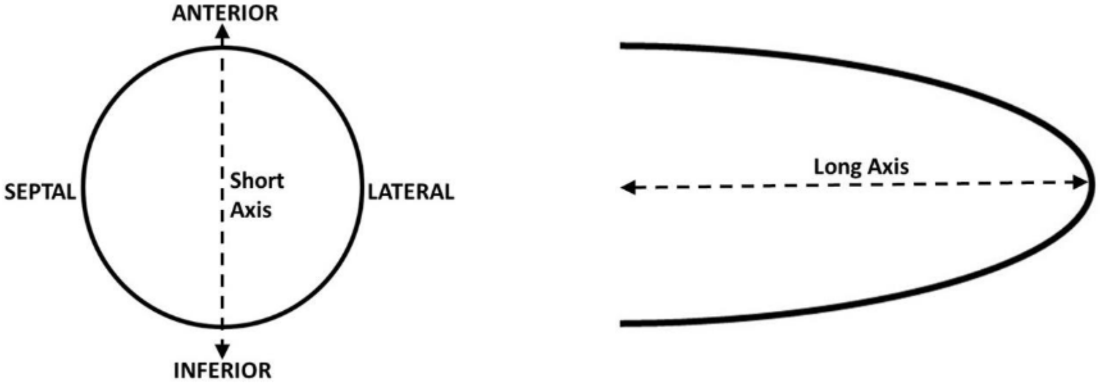

(A) (B)

Figure 2.4. AHA standardized LV model. (A) Short axis view of the left ventricle, shown in the AHA recommended orientation. (B) Vertical long axis view.

To orient the left ventricle in the aforementioned standard, a 3D rotation is performed on the entire volume for each time frame. The volume is first rotated about the Z axis and then about the X axis. The result of the sequence of rotations is that the long axis of the left ventricle will now be oriented parallel to the Y axis as shown in Figure 2.5.

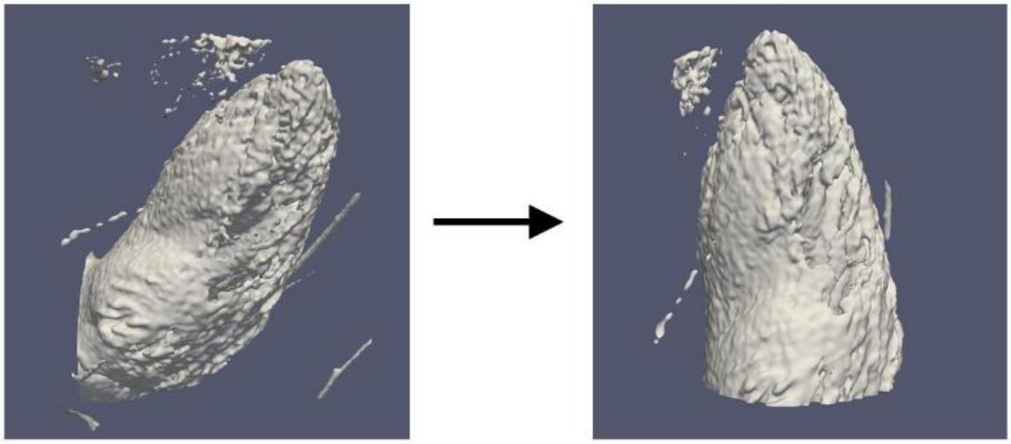

(A) (B)

Figure 2.5. LV matrix rotation process. (A) Unrotated ventricle. (B) Rotated ventricle.

2.1.4 Image Segmentation & Edge Detection

Once the CT images have been rotated as per the recommendations laid out by the AHA, the next step involves segmenting out the ventricle from the rest of the image. Although a rough crop is made around the left ventricle, there still remain coronary arteries, parts of the aorta, etc. which need to be removed. It is worth mentioning here that the image of the ventricle that we see in Figure 2.5 is actually of the blood pool within the ventricle. It is this blood which sis highlighted during the imaging process due to the use of contrast agents. The blood pool takes the shape of the endocardial wall, and hence the endocardial wall can be extracted by detecting the edge of the left ventricular volume.

Consider Figure 2.6. As highlighted in the image, the left ventricle has a Hounsfield unit (measure of radiodensity) of ~500. By applying a minimum threshold value of ~500, all voxels containing values less than the threshold value are set to 0, while all values greater than the threshold value are set to 1 (Chapter 4 contains more information on the selection and sensitivity of the threshold value). Additionally, the algorithm is developed to retain only the single largest connected region. This ensures that arteries and other smaller anatomical features of similar threshold values are removed, while only retaining a continuously connected left ventricular blood pool. The volume of 1's and 0's, with 1's representing points inside the blood pool and 0's outside is called the *Left Ventricular Mask*.

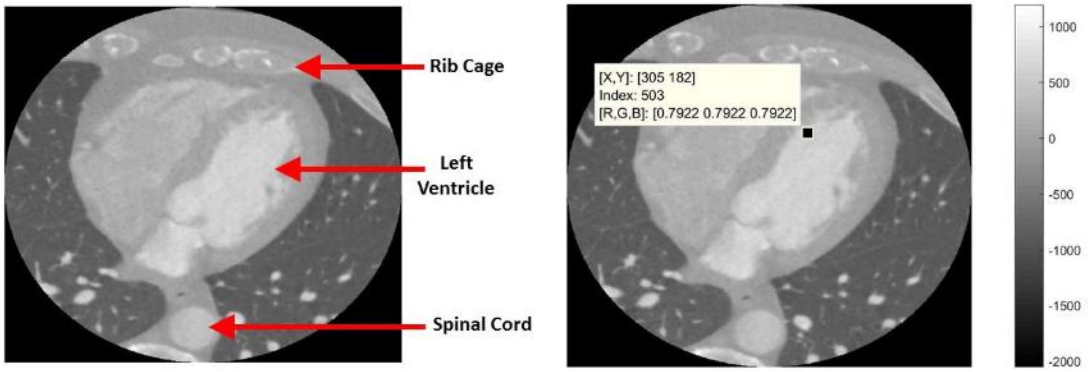

(A) (B)

Figure 2.6. Typical mid-slice of a cardiac CT scan. (A) Mid- slice of a typical cardiac CT scan highlighting the different anatomical parts. (B) Data tip showing an approximate radiodensity value of the left ventricle.

After obtaining the mask, the next step involves detecting the endocardial wall. The endocardial wall contains the trabeculation and papillary muscles and it is the change in structure of these features across the cardiac cycle that are essential for the quantification of regional cardiac function. To detect the endocardial wall, an in-house edge detection algorithm was developed and applied on the mask. The algorithm used a convolution kernel (a 3x3x3 kernel of ones) on the 3-D volume of the left ventricular mask. The result of the convolution process is the detection of the edge (endocardial wall), with a value of 1 representing a point on the edge and a value of 0 elsewhere. Another round of filtering and discarding small disconnected regions was performed, while keeping the single biggest connected edge. The detected endocardial wall is shown in Figure 2.7.

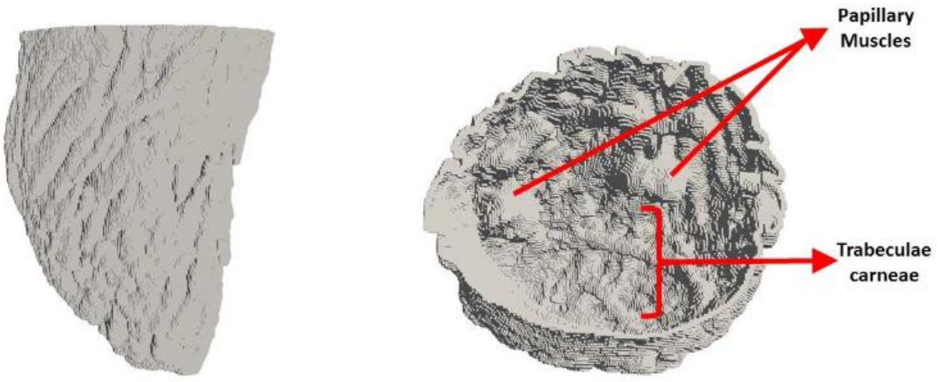

(A) (B)

Figure 2.7. Segmented endocardial wall. (A) Long axis view. (B) Short axis view

2.2 Local Neighborhood Fractal Dimension

The next step after detecting the endocardial wall, is to characterize its local structure through regional values of fractal dimension. This section of the algorithm was performed using *Fortran*, which was approximately two orders of magnitude faster than *Matlab*. To compute these regional values of fractal dimension, a cube of size 64 was chosen to serve as the localized region/neighborhood. In other words, the cube is a subset of the parent set and the fractal dimension is calculated for the section of the endocardial wall contained in that cube. The cube is then displaced in the X,Y, and Z directions, sequentially by 8 units, until the entire volume is covered. At the end of the operation, each cubical region of size 64 is represented by a single value of its fractal dimension, providing information on the regional complexity/roughness of the surface.

The fractal dimension is computed using an in-house developed box-counting algorithm. The box-counting algorithm is the most prevalent among several methods in use today to calculate the fractal dimension of a system [3]. The algorithm calculates the number of boxes, as a function of the size of the box, that are required to completely cover the set, without any of the boxes overlapping. The algorithm is designed to function for powers of 2 because of the simplicity and symmetry in dividing the set. Within a cube of size 64, the box sizes vary from 1 (one voxel) to 32, in powers of 2. This section of the *Fortran* script was parallelized, running multiple processes parallely on different processing cores. The fractal dimension is calculated as per the linear regression model $y = mx + c$, where m is the slope and c is the y-intercept, between the logarithmic ratio of the number of boxes required, as a function of the box size, to the box size. The slope m is the fractal dimension of the set. Mathematically,

$$F_D = m = \frac{\log(N(j))}{-\log(j)},$$

where $N(j)$ is the number of boxes of size j required to completely cover the set without overlap and F_D is the fractal dimension. Figure 2.8 shows the relationship between the number of boxes and box size and the linear fit between them.

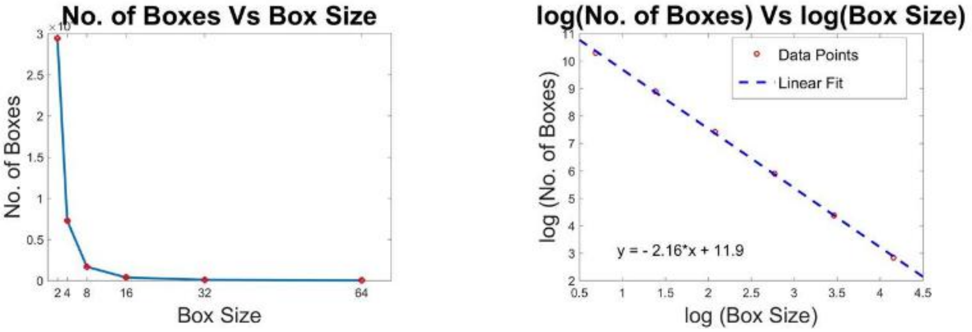

(A) (B)

Figure 2.8. Relationship between no. of boxes and the box size. (A) Linear Scale. (B) Logarithmic Scale, with the linear fit.

2.2.1 Remapping Local Fractal Dimensions onto LV Edge

Each value in the grid of local fractal dimension values is calculated at the center for every location of the neighborhood box. The values represent the regional complexity of the set defined within the particular neighborhood. To characterize every point of the endocardial wall with a fractal dimension, a linear interpolation is performed between the grid of local fractal dimensions and the points defining the edge of the endocardial wall. The final output is shown in Figure 2.9.

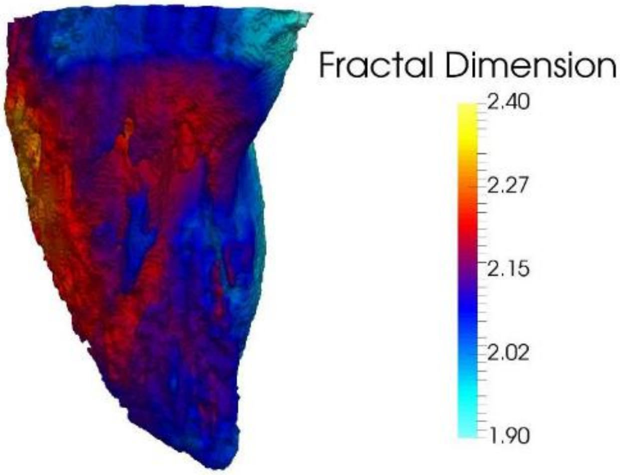

Figure 2.9. Fractal dimensions characterizing the left ventricular endocardial wall.

For example, if the edge defining the endocardium is stored in a cube of size 256 and a neighborhood of size 64 is chosen with a sequential displacement of 8 units, then the grid of local fractal dimension values will be stored in a matrix of size 25x25x25. The values from this grid are linearly interpolated back onto the endocardium, giving a point by point characterization of the endocardial wall structure as shown in Figure 2.9.

2.3 Bullseye Plots

The regional characterization of the endocardium is represented by a 2-D 'bullseye plot', in the format specified by the AHA standardized LV segmentation model [4]. These are circular donut shaped plots where the radial coordinate corresponds to the coordinate along the long axis of the ventricle, transitioning from the apex at the inner circumference of the plot, to the base at the outer circumference. The generation of the plot is explained in Figure 2.10 below. The plot's 12, 3, 6, and 9 o'clock represent the Anterior, Lateral, Inferior, and Septal regions of the left ventricle respectively.

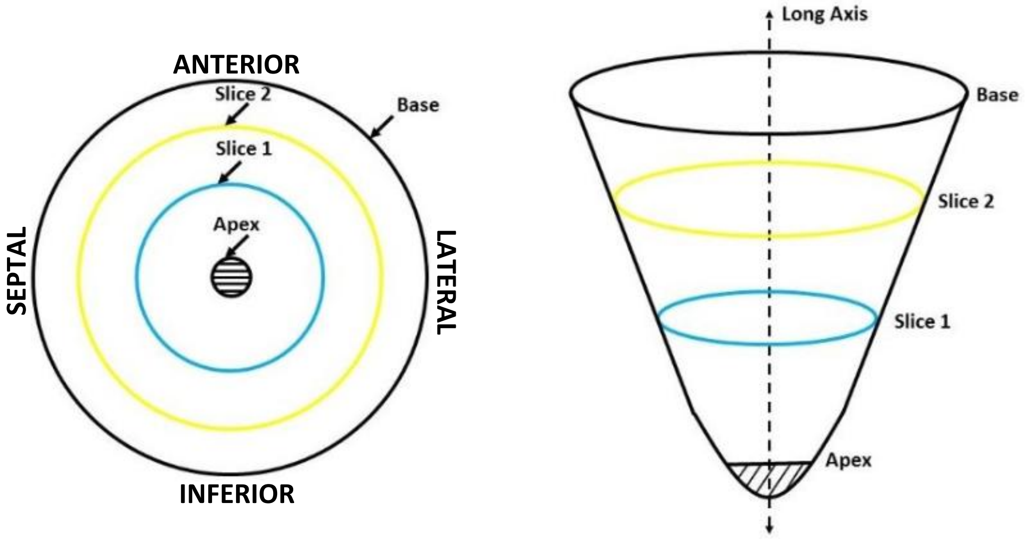

(A) (B)

Figure 2.10. Creation and orientation of the bullseye plot. (A) Representation of corresponding slices of the ventricle on the plot. (B) Long axis view of the ventricle showing the different slices.

References

[1] Daveynin (Artist). (2012) *GE LightSpeed CT scanner* [Digital Image]. Retrieved from Wikimedia Commons website: https://commons.wikimedia.org/wiki/File:UPMCEast_CTscan.jpg

[2] Heller, G. V., Cerqueira, M. D., Weissman, N. J., Dilsizian, V., Jacobs, A. K., Kaul, S., ... & Verani, M. S. (2002). Standardized myocardial segmentation and nomenclature for tomographic imaging of the heart: a statement for healthcare professionals from the Cardiac Imaging Committee of the Council on Clinical Cardiology of the American Heart Association. *Journal of Nuclear Cardiology*, *9*(2), 240-245.

[3] Falconer, K. (2004). *Fractal geometry: mathematical foundations and applications*. John Wiley & Sons.

[4] Heller, G. V., Cerqueira, M. D., Weissman, N. J., Dilsizian, V., Jacobs, A. K., Kaul, S., ... & Verani, M. S. (2002). Standardized myocardial segmentation and nomenclature for tomographic imaging of the heart: a statement for healthcare professionals from the Cardiac Imaging Committee of the Council on Clinical Cardiology of the American Heart Association. *Journal of Nuclear Cardiology*, *9*(2), 240-245.

Chapter 3

RESULTS

This chapter covers the validation and results of the method developed, as described in Chapter 2. The first section deals with validating the box-counting algorithm with standard test fractals whose dimension is known and well documented in literature. The next part summarizes the results of the tool, performed on 10 normal cases and one abnormal case of a patient suffering from heart failure.

3.1 Algorithm Validation

The in-house box-counting algorithm developed was tested on three "2-dimensional" fractals and two "3-dimensional" fractals whose dimensions are well documented in literature. This served as an initial validation of the accuracy of the algorithm and its capability to measure objects with a great degree of variability, viz. the left ventricle.

3.1.1 Julia Set

The Julia set was the first fractal the algorithm was tested on. The image was generated through an iterative process using the equation $z^2 + c$, where c is a parameter that gives us different variations of the Julia set.

a) The first variation of the Julia set was generated using a value of *c = -1*. Figure 3.1 shows a section of the Julia set. The theoretical fractal dimension is reported in literature to be 1.27 (rounding to the nearest hundredth). The dimension calculated by the box-counting algorithm was 1.23, an error of 3%. The error is due to the limited resolution (memory constraints) and numerical noise.

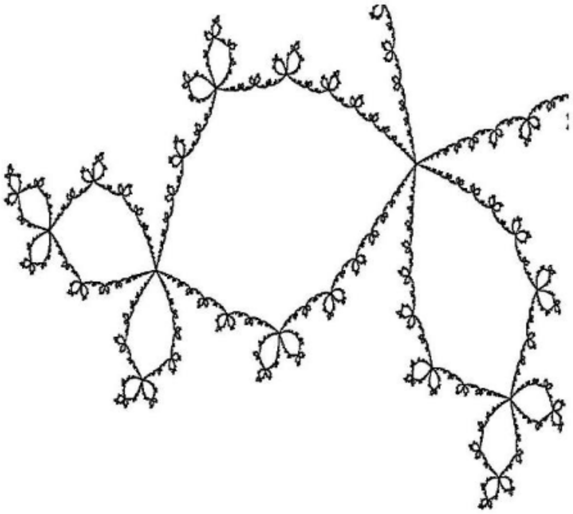

Figure 3.1. A section of the Julia Set (c = -1).

Table 3.1. Theoretical and computed fractal dimension values for Julia Set (c = -1)

Theoretical Fractal Dimension	***Computed Fractal Dimension***	***Error %***
1.27	1.23	3

b) The second variation of Julia set was generated using a value of *c = -0.123 + 0.7i*. Figure 3.2 shows a section of the Julia Set (c = -0.123 + 0.7i). The theoretical fractal dimension is reported in literature to be 1.39 (rounding to the nearest hundredth). The dimension calculated by the box-counting algorithm was 1.37, an error of 1.4%. As mentioned above, the error arises due to a limitation in the resolution of the set as well as numerical noise in the algorithm.

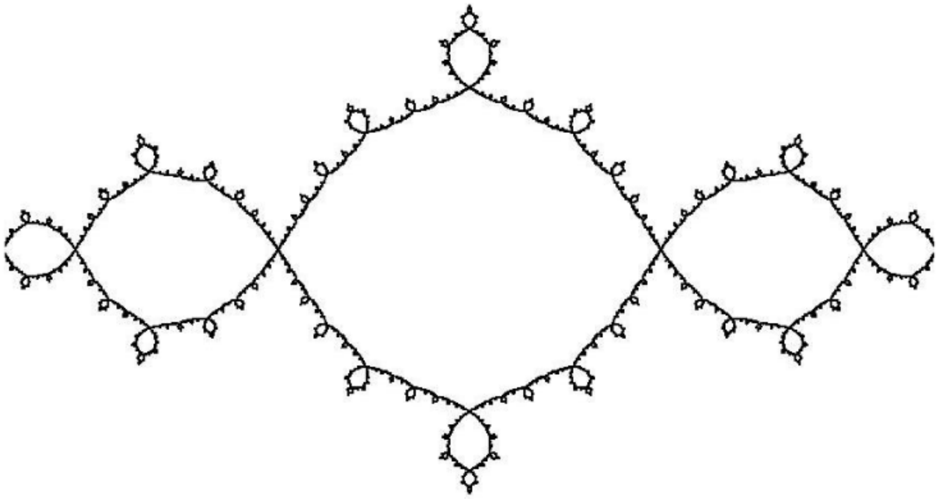

Figure 3.2. Julia Set (c = -0.123 + 0.7i).

Table 3.2. Theoretical and computed fractal dimension values for Julia Set (c = -0.123+0.7i)

Theoretical Fractal Dimension	***Computed Fractal Dimension***	***Error %***
1.39	1.37	1.4

3.1.2 Sierpinski Triangle

The Sierpinski Triangle is another example of a fractal generated through an iterative process. The set is created starting from a whole equilateral triangle and dividing each of its line segments into equal halves recursively and joining the three mid-points to form 4 sub-triangles, as shown in Figure 3.3. Of the 4 sub-triangles created, the middle triangle is removed leaving only three sub-triangles. Therefore, with every iteration of dividing each line segment by one half, three triangles are created.

Area and length parameters of the Sierpinski Triangle have already been discussed in section 2.3 of Chapter 2. Mathematically, $2^d = 3$, where d is the dimension of the set. The equation yields a value of $d = 1.58$. The dimension calculated by the box-counting algorithm was 1.58.

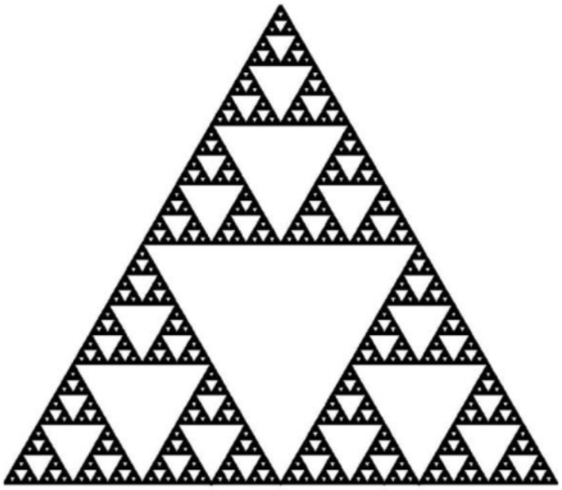

Figure 3.3. Sierpinski Triangle.

Table 3.3. Theoretical and computed fractal dimension values for Sierpinski Triangle

Theoretical Fractal Dimension	***Computed Fractal Dimension***	***Error %***
1.58	1.58	0

3.1.3 Menger Sponge

The Menger sponge is a 3-D generalization of the Cantor set [1]. It is an example of a fractal which is neither 2-D nor 3-D, but has a dimension in between 2 and 3. The Menger sponge is shown in Figure 3.4. It is generated by dividing each side of a cube into 3 equal parts, which generates 27 equal sub-cubes. The middle cube of each face as well as the central cube of the whole structure is removed at each iteration, leaving only 20 sub-cubes remaining. The volume at the end of each iteration is therefore $\left(\frac{20}{27}\right)^n$, which tends to zero as n becomes very large. However, the surface area, given by the relation $2\left(\frac{20}{9}\right)^n + 4\left(\frac{8}{9}\right)^n$, tends to infinity as n increases, making the set neither a true plane nor a true volume. Mathematically, due to the creation of 20 sub-cubes with a scaling factor of $\frac{1}{3}$, the dimension of the Menger sponge is represented by the equation $3^d = 20$, where d is the dimension. The equation yields a value of $d = 2.72$. The dimension calculated by the box-counting algorithm was 2.72.

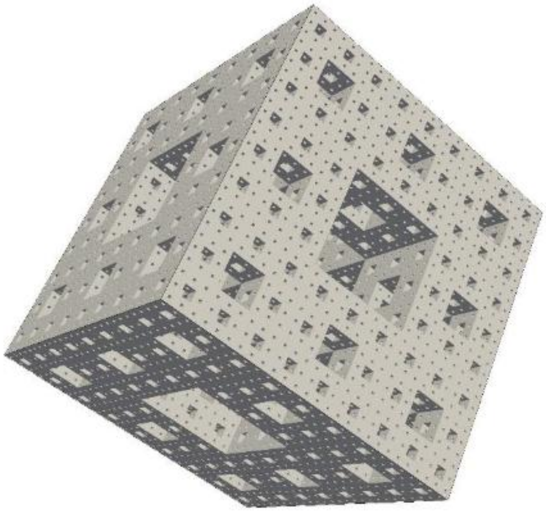

Figure 3.4. Menger Sponge.

Table 3.4. Theoretical and computed fractal dimension values for Menger Sponge

Theoretical Fractal Dimension	***Computed Fractal Dimension***	***Error %***
2.72	2.72	0

3.1.4 3-Dimensional Cantor Dust

The 3-D Cantor Dust was the last fractal the algorithm was tested on. The fractal was generated using a probability of 0.7. The probability parameter determines the filling characteristics for the random generation of the points in the set. The Cantor dust is shown in Figure 3.5. The theoretical dimension is given by the formula $Dim = D + \frac{logP}{log2}$, where P is the probability and D is the general dimension of the fractal, in this case being 3. With a value of $P = 0.7$, the equation yields a value of $Dim = 2.48$. The dimension calculated by the box-counting algorithm was 2.49.

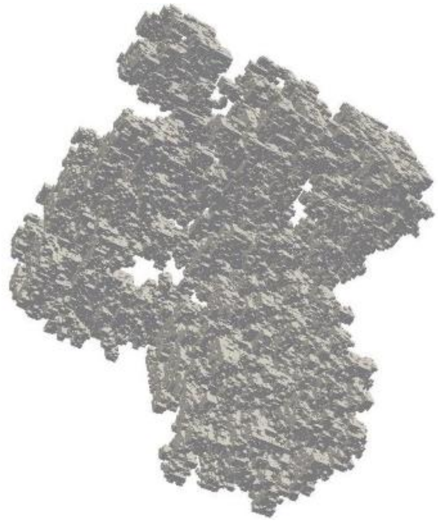

Figure 3.5. 3-D Cantor Dust.

Table 3.5. Theoretical and computed fractal dimension values for 3-D Cantor Dust

Theoretical Fractal Dimension	***Computed Fractal Dimension***	***Error %***
2.48	2.49	0.4

The validation of the algorithm with the above set of standard fractals shows a good degree of accuracy of the method. Unfortunately, there is no known documented literature to validate the calculation of the local fractal dimension. However, in principle, we can extend the method to calculate local values of fractal dimension as it is the same algorithm only applied region-wise across the set.

3.2 Application to Human Cardiac CT Scans

At the time of publication of this thesis, we had access to 10 data sets of normal patients with no known cardiac dysfunction and one data set of a patient suffering from heart failure. The patient suffering from heart failure had a pacemaker implanted with one lead attached to the apex of the right ventricle and the other lead attached to the right atrium. The data sets used were jointly owned by Dr. Elliot R. McVeigh, UC San Diego and by Dr. Chen of the National Institutes of Health. Each data set was analyzed as per the method specified in Chapter 2 of this thesis.

The following images show the regional characterization of the left ventricular endocardium through its fractal dimension for 10 normal patients and the one patient suffering from heart failure. The plots for each patient are arranged from left to right depicting different stages of the cardiac cycle: End diastole, early systole, mid systole, end systole, mid-filling, and diastasis.

3.2.1 Normal Cases

The bullseye plots for the 10 normal cases are shown in Figure 3.6 below. It is visible from all 10 cases below that the regional values of fractal dimension decrease from end diastole(ED) to end systole(ES). This agrees with the variation in the structure of the trabeculae carneae of the endocardium; they expand out towards ED and contract towards ES. On the right is a graph showing the variation in left ventricular volume as a function of the cardiac cycle for each patient.

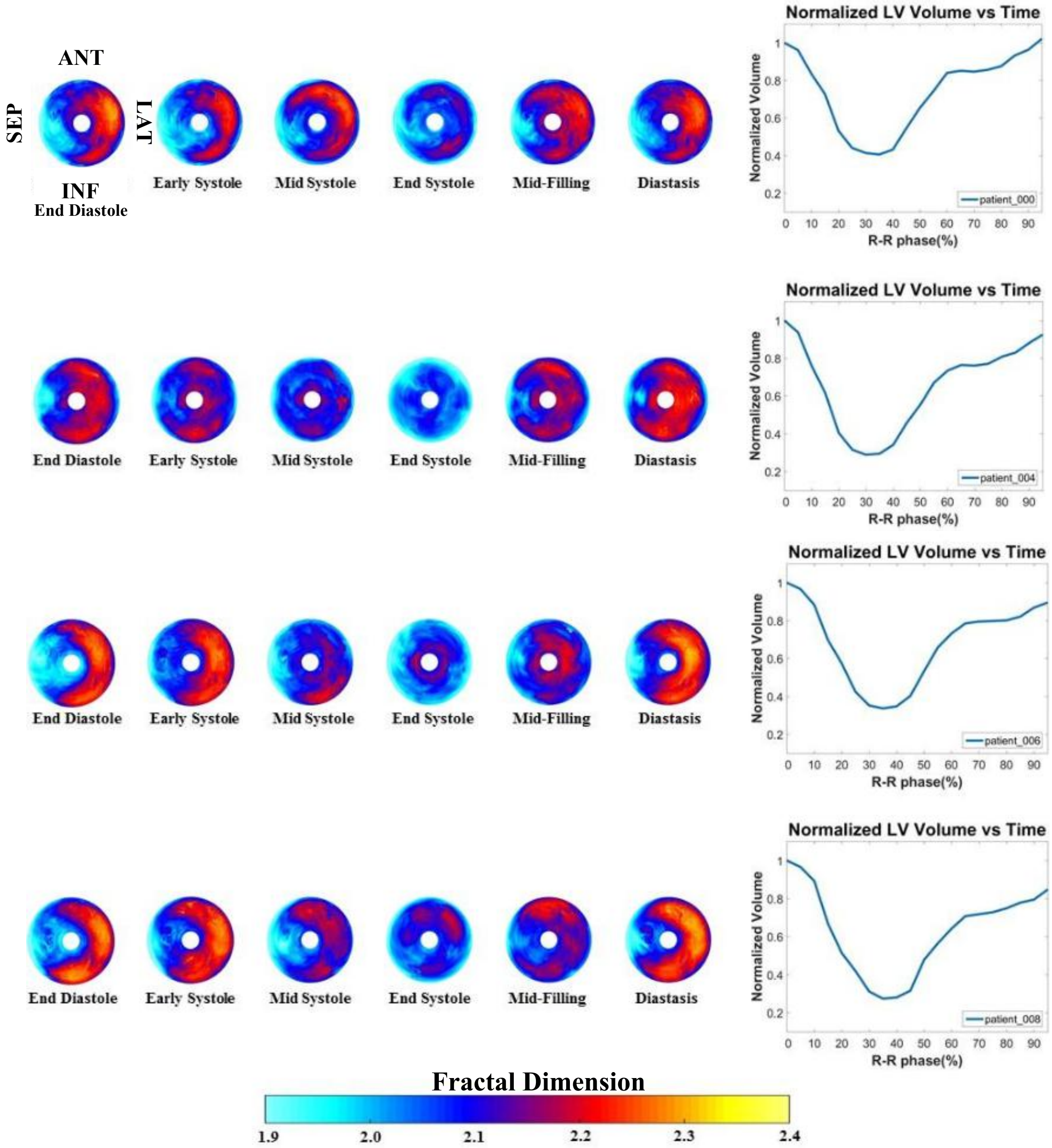

Figure 3.6. Results of the analysis for 10 normal cases. Each patient has 6 bullseye plots depicting different stages across one cardiac cycle and one volume plot on the right. The bullseye plots show the regional surface characterization of the left ventricular endocardium through its fractal dimension, whose scale is represented in the color bar. It is visible from the cases above & below that the endocardial surface smooths out towards end systole and assumes a more complex structure towards end diastole, due to the compaction and expansion of the endocardial trabeculae respectively. The graph on the right shows the variation of the normalized left ventricular volume across one cardiac cycle.

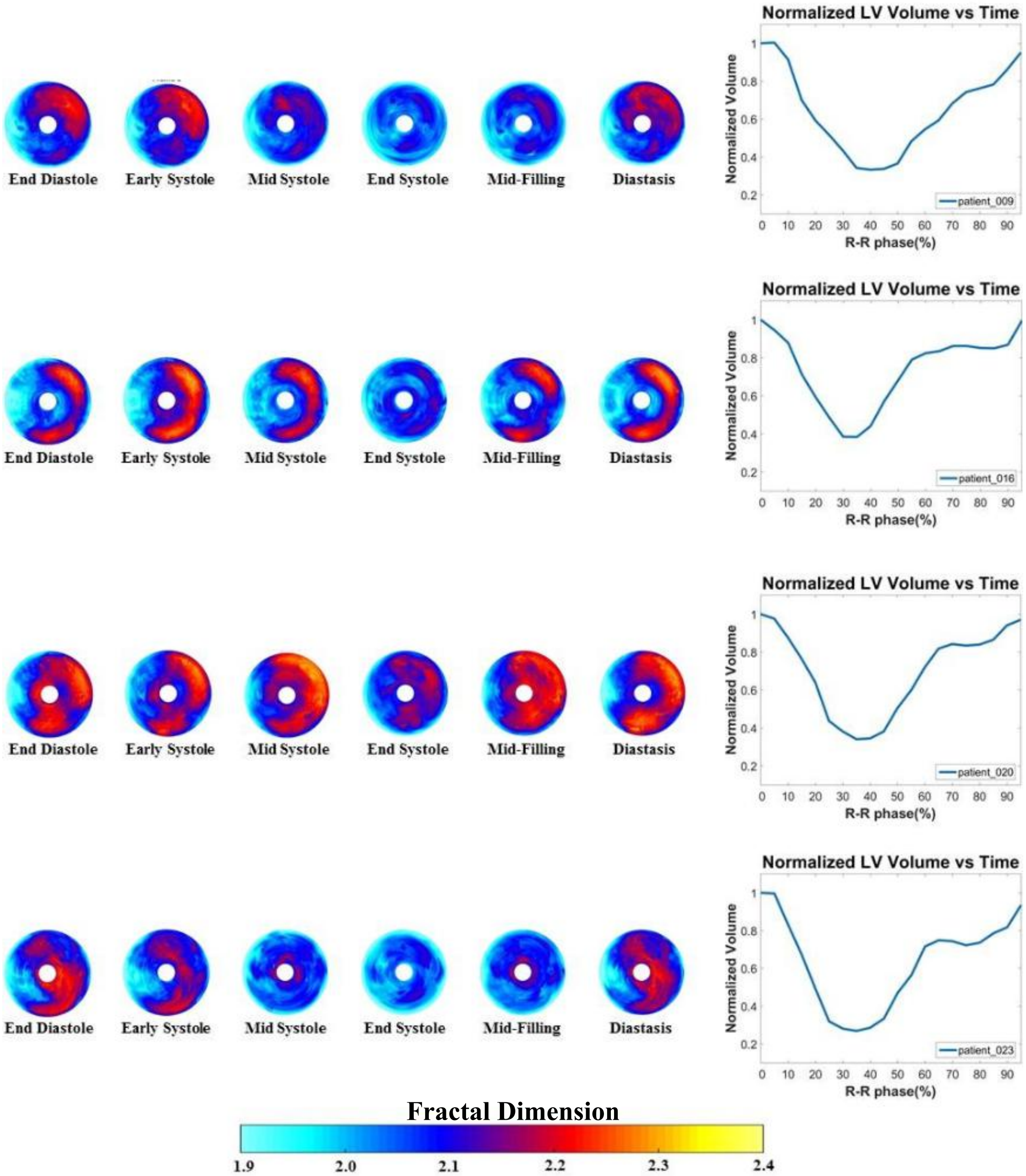

Figure 3.6. Results of the analysis for 10 normal cases. Each patient has 6 bullseye plots depicting different stages across one cardiac cycle and one volume plot on the right. The bullseye plots show the regional surface characterization of the left ventricular endocardium through its fractal dimension, whose scale is represented in the color bar. It is visible from the cases above & below that the endocardial surface smooths out towards end systole and assumes a more complex structure towards end diastole, due to the compaction and expansion of the endocardial trabeculae respectively. The graph on the right shows the variation of the normalized left ventricular volume across one cardiac cycle, Continued

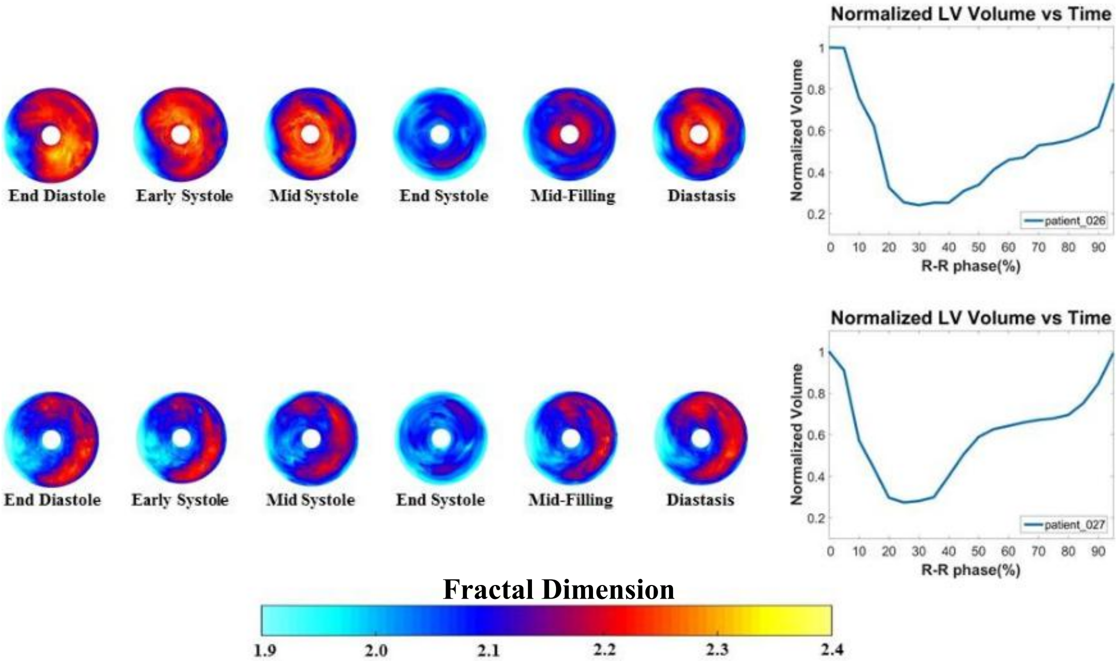

Figure 3.6. Results of the analysis for 10 normal cases. Each patient has 6 bullseye plots depicting different stages across one cardiac cycle and one volume plot on the right. The bullseye plots show the regional surface characterization of the left ventricular endocardium through its fractal dimension, whose scale is represented in the color bar. It is visible from the cases above & below that the endocardial surface smooths out towards end systole and assumes a more complex structure towards end diastole, due to the compaction and expansion of the endocardial trabeculae respectively. The graph on the right shows the variation of the normalized left ventricular volume across one cardiac cycle, Continued.

3.2.2 Heart Failure Case

The analysis was performed on the CT scan of a patient suffering from heart failure. The patient was implanted with a pacemaker and two leads, one attached to the right ventricle and the other to the right atrium as shown in Figure 3.7. The presence of the metallic pacemaker lead made the segmentation of the left ventricle more involved, due to the reflection from the metal during imaging.

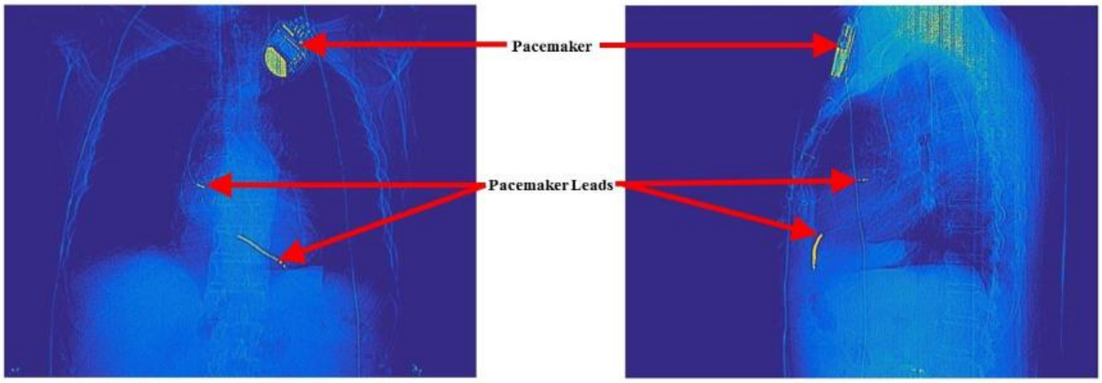

(A) (B)

Figure 3.7. CT images of the patient implanted with a pacemaker. (A) Front view, showing the pacemaker device at the top (near the collar bone) and the two leads. (B) Left view.

The reflection created a small bridge-like section of pixels with radiodensity values higher than the values possessed by the left ventricular blood pool, as shown in Figure 3.8. Thus, on applying a threshold value, the bridge-like section was still present and needed to be manually cut using a plane.

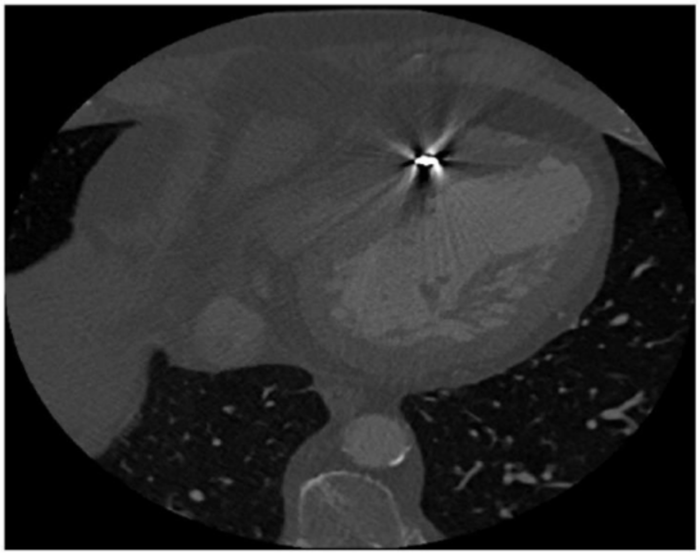

Figure 3.8. Slice of the CT scan showing the high radiodensity reflection from the pacemaker lead.

The bullseye plots for different stages of the cardiac cycle and the corresponding graph depicting variation of left ventricular volume as a function of the cardiac cycle is shown below in Figure 3.9. Unlike the 10 normal cases shown in Figure 3.7, there is no considerable change in the "roughness" or structure of the endocardium across the cardiac cycle. In other words, the trabeculae carneae undergo suppressed cycles of compaction and expansion.

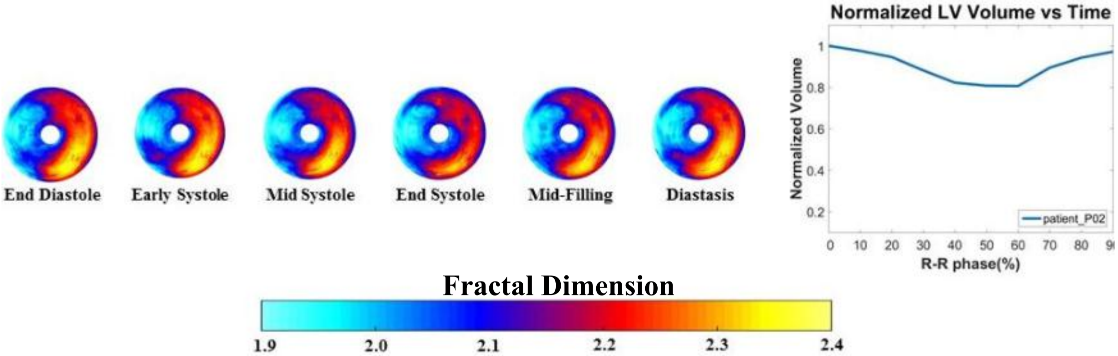

Figure 3.9. Results of the analysis of the patient suffering from heart failure. Unlike the 10 normal cases, there is no considerable change in the surface characterization of the endocardium across the cardiac cycle. The graph on the right shows the variation of the normalized left ventricular volume across one cardiac cycle. The volume changes marginally due to suppressed cardiac function.

The difference between the normal cases and the one heart failure case is visible from Figures 3.6 and 3.9. While the normal hearts get compacted towards end systole, giving a smooth structure to the endocardium, the heart failure case shows a suppressed degree of compaction of the trabeculae, which is a result of the suppressed heart function. Thus, through the surface characterization of the endocardial surface by its fractal dimension, the method is able to distinguish between normal and abnormal hearts.

3.3 Quantification of Cardiac Function

The visual differences between the normal and abnormal cases as shown in Figures 3.6 and 3.9 were quantified using the *relative change* between the sum of the local fractal dimension values between end diastole(ED) and end systole(ES). Mathematically, for each patient

$$Relative\ Change = \frac{sum(ED) - sum(ES)}{sum(ED)}.$$

Figure 3.10 shows a boxplot of the relative change in fractal dimensions for the two groups. The normal cases had a median value of 0.137, while the median (only) value of the heart failure case was 0.002. The standard deviation for the normal cases was 0.058. This preliminary statistical analysis shows a marked difference between the behavior of the normal and abnormal cases. The relative change for the abnormal case was two orders of magnitude different from the median value for the normal cases.

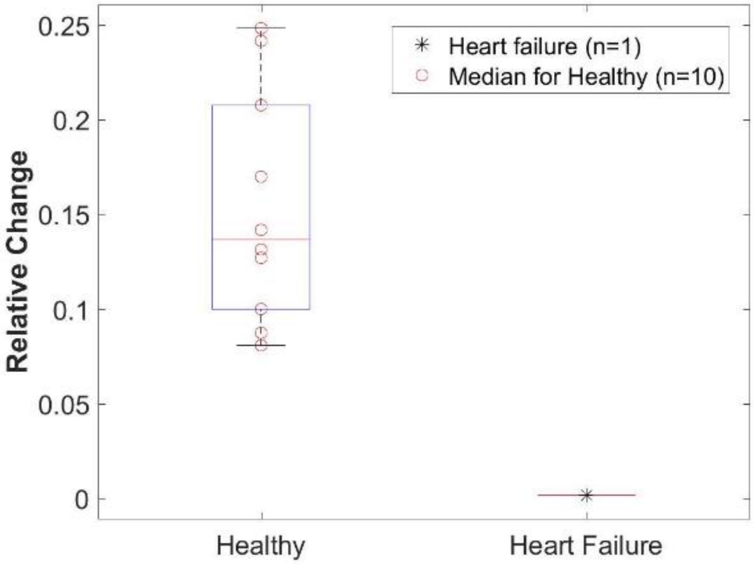

Figure 3.10. Relative change in the sum of the local fractal dimensions of all points on the endocardial surface between end diastole and end systole.

3.4 Local Neighborhood Size Sensitivity Analysis

The local neighborhood cube size of 64 was initially chosen on two grounds:

a. It provides a sufficient number (6) of data points to calculate the best fit (linear regression) slope of the curve.

b. A cube of size 64 is large enough to capture the complexity of the trabeculae (~30 voxels in length) while still being small enough (1/64th the volume of the parent matrix of size 256^3) to provide a regional characterization of the endocardium.

However, it was necessary to understand the sensitivity of the method to the box size and to gain insight on the fractal nature of the endocardium at different scales.

As specified in Chapter 2, the in-house developed box-counting algorithm functions in powers of 2 for simplicity. The 3-D matrix storing the endocardium was padded to have a uniform cube size of 256, or 2^8. The algorithm calculates the fractal dimension by determining the best fit slope between the logarithmic ratio of the number of boxes of a certain size required to cover the entire set, to the box size. Each neighborhood cube of size 2^n provides *n* number of points to fit the curve, and hence the size of the local neighborhood cannot go below 2^2 (a minimum of two points required to fit a curve), that is a cube of size 4. On the other hand, as the 3-D volume of the endocardial surface is stored in a matrix of size 256, the permissible upper limit for the neighborhood is a cube of size 128. Using a box size of 256 will measure only one value of the fractal dimension for the structure of the endocardium as a whole.

An analysis was performed on a sample normal case and the heart failure case for all possible neighborhood box sizes; 4, 8, 16, 32, 64, and 128. The results of the analysis are shown below in Figure 3.11, in the form of bullseye plots of the endocardium at end diastole and end systole for each category.

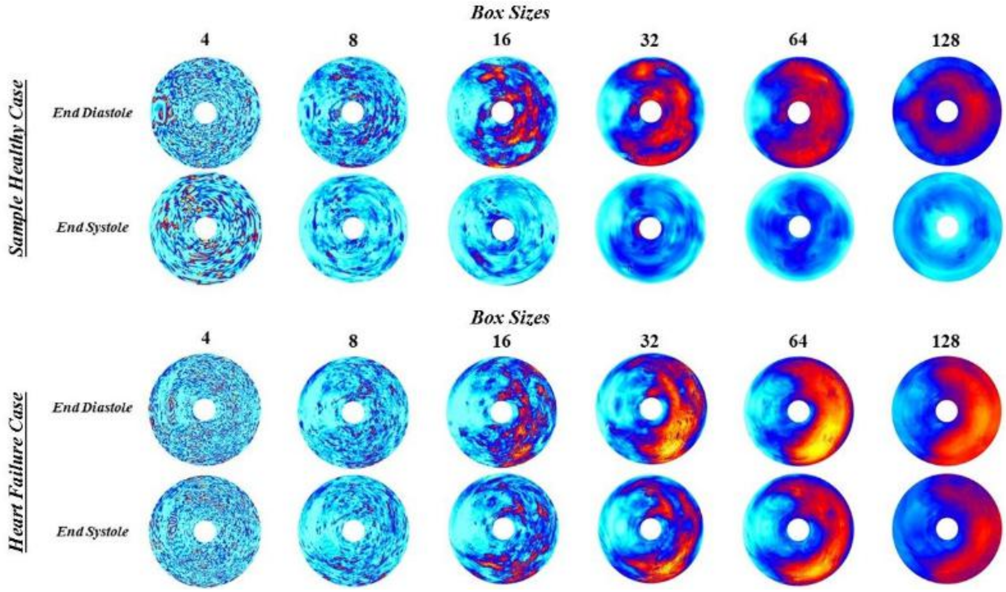

Figure 3.11. Bullseye plots at end diastole and end systole for different box sizes of the local neighborhood. (Above) Sample normal case. (Below) Heart failure case.

The size of the neighborhood behaves in a manner like the resolution of an image. From Figure 3.11, it is seen that as the size of the neighborhood is increased (lower resolution), the bullseye plots assume a more uniform and smooth variation in the local values of the fractal dimension. At the smaller sizes (finer resolution), the local fractal dimension values are more localized to few pixels. Other than the neighborhood of size 4, corresponding regions of higher fractal dimensions are detected consistently by neighborhood sizes of 8, 16, 32, 64, and 128. The neighborhood size of 4 has an inherent limitation in the fact that it has only two points to fit the curve. Additionally, the fractal nature of the endocardium may break at such fine scales and a combination of the above two factors is probably the cause for the random distribution of pixels in the bullseye plots for a size of 4.

Unfortunately, there is no gold standard to compare the different sizes and state that one size is better than the other. Depending on the requirements of the user, the different neighborhood sizes provide a different resolution to characterize the endocardium. Neither size is right nor wrong. If the user is interested in understanding the structural complexity of the endocardium at finer length scales, using a smaller neighborhood size is recommended. On the other hand, if the user is interested in studying the contractility of different regions of the heart on a more macro level, as in the case of the patient suffering from a heart failure, a box size of 64 or 128 would be ideal. It is worth mentioning that as the neighborhood size is increased, the computation time increases as well. The analysis of one time frame using a neighborhood size of 4 takes ~0.7 seconds, whereas the analysis using a neighborhood size of 128 takes ~90 seconds.

The relative change between the sum of all local fractal dimension values at end diastole and end systole was calculated for the sample normal case and the heart failure case. The boxplot is shown in Figure 3.12. Although the neighborhood size of 4 does not generate a visually consistent map of local fractal dimensions, it was able to differentiate between the normal cases and the patient with heart failure. The relative change value for the abnormal case was 3.1, 2.9, 2.8, 2.8, 2.6, and 2.8 standard deviations away from the corresponding mean of the normal cases for each of the neighborhood sizes of 4, 8, 16, 32, 64, and 128 respectively.

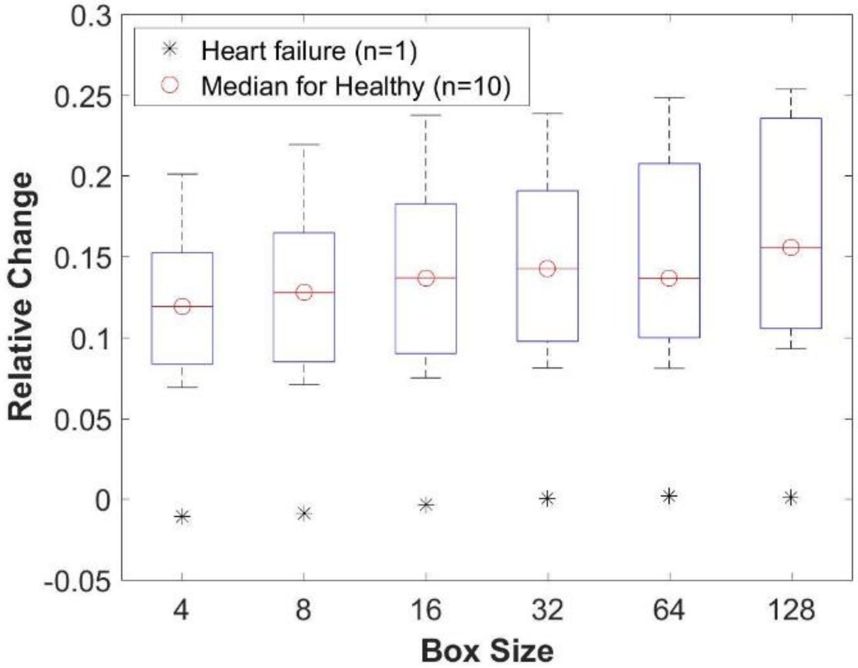

Figure 3.12. Relative change between the sum of all local fractal dimension values on the endocardial surface at end diastole and end systole for 10 normal cases and the one patient suffering from heart failure.

At very small length scales, such as those measured with a neighborhood of size 4, with only two points to calculate the fractal dimension, it is uncertain if the method is measuring the fractal nature of the set or just providing a crude measure of its "*roughness*". However, Figure 3.12 shows that maybe the true fractal dimension is not necessary to quantify regional cardiac function and a simpler measure of just the "*roughness*" of the endocardium would suffice. The hypothesis remains the same, abnormal change in the structural complexity of the endocardium, which is a result of the insufficient or abnormal compaction and expansion of the trabeculae carneae, could be used to identify regions of abnormal contractility.

3.5 Threshold Sensitivity Analysis

The method proposed and developed in this thesis is reliant on the observer to input an initial threshold value to segment out the left ventricle from the cardiothoracic CT scan. The process of thresholding and segmentation is described in Chapter 2. The value chosen is subjective, and may vary among different observers. In practice, the CT scans are read by radiologists and inter-observer variability among them maybe low. In this section, the method is analyzed to understand its sensitivity to the initial threshold chosen. Additionally, a study was conducted using three independent observers to assess the inter-observer variability in the choice of the initial threshold value.

There is only a specific range of threshold values within which there can exist inter-observer variability. Beyond this range, the left ventricle will either be over-represented or under-represented depending on whether the threshold chosen was either too low or too high respectively. Figure 3.13 shows three different structural representations of the same left ventricle with a low, moderate, and high threshold value. From Figure 3.13, it is observed that too low or too high a value of the threshold does not provide an accurate anatomical model of the left ventricle. These limits were determined through visual inspection and the sensitivity of the method was tested for a range of threshold values that lay between these extreme limits. Unfortunately, there is no gold standard for the selection of the threshold and the value chosen by one observer is neither ‘right’ nor ‘wrong’ when compared to the value chosen by another observer. Therefore, the study is aimed at assessing the dependence of the result of the method (the fractal dimension) on the choice of the threshold value and not on determining what the ‘right’ threshold value is.

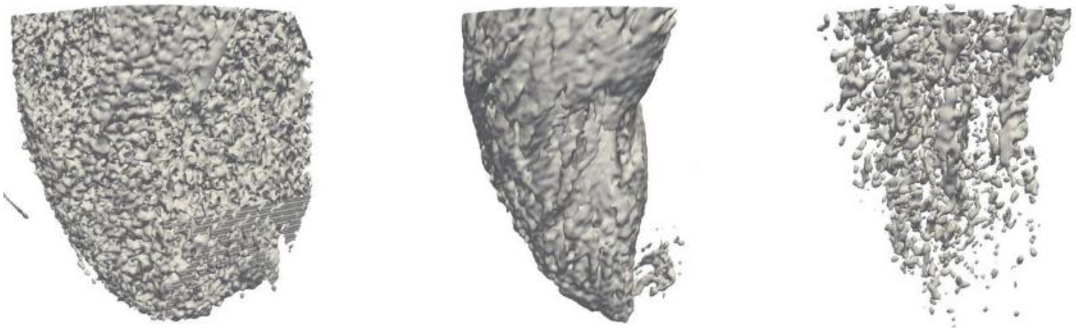
(A) (B) (C)

Figure 3.13. 3-D view of a human left ventricle for different threshold values. (A) Threshold value too low; over represents the left ventricle. (B) Acceptable threshold value; represents the true anatomy of the left ventricle. (C) Threshold value too high; under represents the left ventricle.

The variations in the quality of the CT scans do not permit a single uniform analysis; instead each CT scan must be analyzed independently. Some CT scans possess noisier signals than others, some may have better spatial resolutions while others may have better temporal resolutions. Each of the 10 normal sets and the one abnormal set was analyzed independently for a range of 11 different threshold values as shown below in Table 3.6. The threshold range for each set, except for set ‘P02’, was chosen based on a ‘center’ value and ±200 HU around the center value, in increments/decrements of 25 HU, except for the extreme values which are off by ±100 HU from the penultimate values on either end respectively. For example, if the center value was chosen to be 500

HU, the values chosen for the sensitivity study were 300, 400, 425, 450, 475, 500, 525, 550, 575, 600, and 700. The set P02 deviated from the above trend because the interval between over representation and under representation of the left ventricle was much shorter, providing fewer sample threshold values in-between.

Table 3.6 Range of threshold values for each patient

Patient Set	**Range of Threshold Values (HU)**
P000	250, 350, 375, 400, 425, 450, 475, 500, 525, 550, 650
P004	200, 300, 325, 350, 375, 400, 425, 450, 475, 500, 600
P006	200, 300, 325, 350, 375, 400, 425, 450, 475, 500, 600
P008	100, 200, 225, 250, 275, 300, 325, 350, 375, 400, 500
P009	100, 200, 225, 250, 275, 300, 325, 350, 375, 400, 500
P016	100, 200, 225, 250, 275, 300, 325, 350, 375, 400, 500
P020	50, 150, 175, 200, 225, 250, 275, 300, 325, 350, 450
P023	300, 400, 425, 450, 475, 500, 525, 550, 575, 600, 700
P026	75, 175, 200, 225, 250, 275, 300, 325, 350, 375, 475
P027	100, 200, 225, 250, 275, 300, 325, 350, 375, 400, 500
P02	75, 125, 175, 200, 225, 250, 275, 300, 325, 350, 375

To save computational time and expense, and also for the easier interpretation of the results, the fractal dimension of the left ventricular endocardium was calculated as a whole. Calculating the local values of the fractal dimension would add another degree of variability and was inessential to the aim of the study. Different values of the initial threshold would result in different structural interpretations of the endocardium, and assessing this variability in structure on a global scale would provide the necessary information on the sensitivity of the method to the initial threshold.

The fractal dimension of the endocardium as a whole was calculated at end diastole for all threshold values in the specified range for each patient. The process adopted was the same as that specified in Chapter 2. The left ventricle is segmented out using each of the threshold values specified in the range and for each case a mask was created with 1's describing points inside the left ventricle (left ventricular blood pool) and 0's outside. The edge of each mask created was detected and the fractal dimension of this edge (endocardium) was calculated for only one phase of the cardiac cycle (end diastole).

Figure 3.14 shows the variation of the fractal dimension calculated at end diastole as a function of the threshold for patient 004. The plot shows a region with no significant change in the fractal dimension between threshold values of 350 and 500. This signifies that the segmented endocardial structure does not change appreciably within this range. For this study, a change greater than 1% was considered significant. In principle, the window of fractal dimension values with less than 1% change between one another can provide the observer with the necessary information to select and input an initial threshold value. It also determines, for each independent patient set, the range of threshold values within which the method is not significantly sensitive.

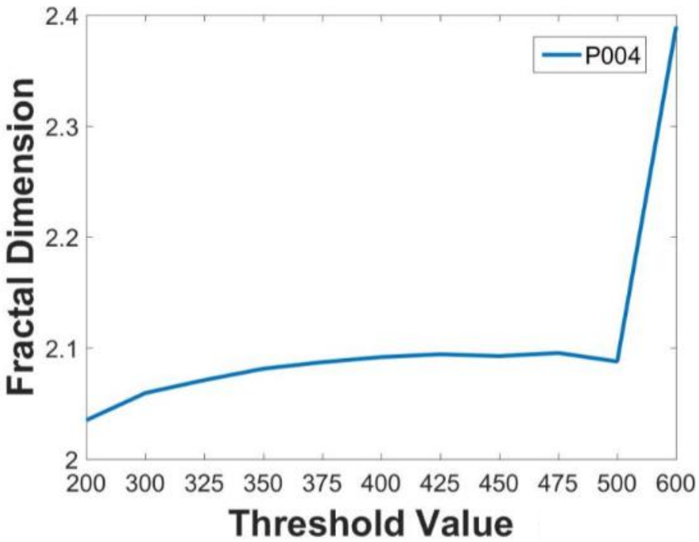

Figure 3.14. Graph depicting the variation in the fractal dimension of the segmented endocardium for patient 004 at end diastole, as a function of the initial threshold value.

For each patient set, the magnitude of the percent change was calculated between successive fractal dimension values. For example, in Figure 3.14, the percent change was calculated between the fractal dimensions at thresholds 300 and 200, 325 and 300, 350 and 325, and so on. Therefore, there would be 10 values of percent change between the 11 different fractal dimensions. Figure 3.15 shows the results of the threshold sensitivity analysis for all 11 patient data sets. It depicts the variation in the percent change of the fractal dimension for successive pairs of threshold values. It is observed from the figure that every patient data set has a region of very small change (< 1%) between successive values of fractal dimension. This region generally occurs in the center portion of the graph due to the manner in which the range of threshold values was chosen and set up. If the observer chooses initial values of the threshold which lie within this range, the method is not significantly sensitive and the results will be consistent with one another.

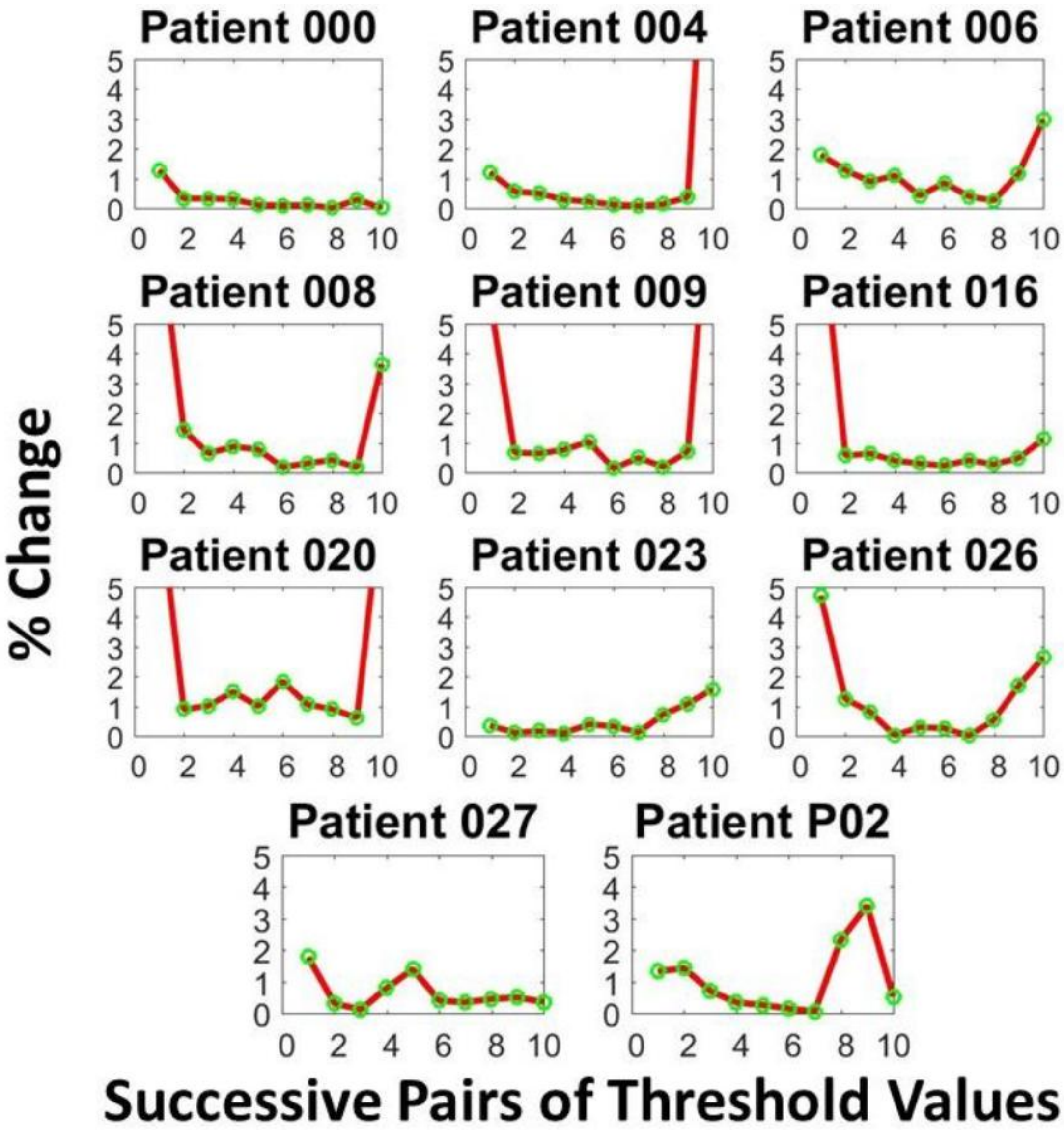

Figure 3.15. Threshold Sensitivity Analysis for all 11 patients. Each graph, for each patient, represents the magnitude of the percent change between successive values of fractal dimension calculated at end diastole for each of the 11 different thresholds specified in Table 3.6. The X axis has 10 points; each point represents a pair of successive threshold values.

Three members were used to assess the inter-observer variability in the selection of the initial threshold value. Two observers were familiar and had prior experience with cardiothoracic CT scans while one observer was viewing the scans for the first time. The observers viewed the scans through OsiriX, an image processing application especially suited for DICOM files. The application allows the user to apply a threshold value and get a preview of the segmented region slice by slice. The values chosen by each of the three observers were recorded for all 11 cases of patient data. The average of the values chosen for each patient is presented in Table 3.7. The mean of the standard deviations calculated for each of the 11 cases was 36.7 HU, which shows a good degree of agreement in the selection of the initial threshold among different observers. It is worth mentioning that neither of the observers were trained in the visual inspection of cardiothoracic scans, and in practice the variability in the selection of the initial threshold among radiologists maybe even lower.

Table 3.7. Summary of the Avg. & std. deviation of the chosen threshold value for each patient

Patient Set	Avg. Threshold Value	Std. Deviation
P000	400	71.2
P004	367	47.6
P006	384	62.5
P008	317	23.1
P009	284	24.1
P016	334	22.6
P020	284	22.6
P023	417	85.6
P026	275	20.4
P027	300	0.9
P02	233	23.8

From Table 3.7, except for patients 000, 004, 006, and 023, it is observed that the standard deviations among untrained observers were consistently low. When examining the graphs of the aforementioned patients in Figure 3.15, it is seen that each of them have large regions of no significant change in the fractal dimension between consecutive threshold values. This possibly occurs due to the relatively good quality of the CT image with minimal signal noise. This also highlights the ability of the method to deal with scans of varying quality.

References

[1] Menger, Karl (1926), "Allgemeine Räume und Cartesische Räume. I.", *Communications to the Amsterdam Academy of Sciences* English translation reprinted in Edgar, Gerald A., ed. (2004), *Classics on fractals*, Studies in Nonlinearity, Westview Press.

Chapter 4

CONCLUSIONS

The primary objective of developing the method was to introduce a non-invasive technique to quantitatively assess regional left ventricular function which is quick, easy to use and minimizes patient discomfort. The most prevalent method in use today relies solely on the operator's subjective visual analysis of cardiac function. Recent techniques have been developed to quantify regional left ventricular function using metrics such as regional strain, wall thickening, etc. These methods rely on computationally intensive algorithms, are time consuming, and may rely on the expertise of the operator.

The method proposed is based on quantifying the changing structure of the left ventricular endocardium across the cardiac cycle. The endocardium is lined with muscular ridges called trabeculae carneae and these ridges open out and contract towards end diastole and end systole respectively. The metric used to quantify the change in the structural complexity of the endocardial wall is the fractal dimension. The fractal dimension is a measure of irregularity of a surface and can distinguish between objects based on their structure.

An in-house box-counting algorithm was developed to calculate the fractal dimension. The algorithm was first validated on a set of three 2-dimensional and two 3-dimensional standard fractals whose dimensions are documented in the literature. The algorithm matched the theoretical dimensions with a great degree of accuracy. The errors in the computed dimensions for the Julia Set ($c = -1$), Julia Set ($c = -0.123 + 0.7i$), Sierpinski Triangle, Menger Sponge, and 3-D Cantor Dust were 3, 1.4, 0, 0, and 0.4% respectively.

To quantify the regional structure of the endocardial wall, the fractal dimension is calculated for defined local neighborhoods. The standard local neighborhood used was a cube of size 64. The fractal dimension for the portion of the endocardial wall contained within this local neighborhood was calculated using the same box-counting algorithm. The method was used to analyze the CT scans of 10 normal cases and one patient implanted with a pacemaker, suffering from heart failure. The bullseye plots for the normal cases showed a uniform decrease in the values of the local fractal dimensions from end diastole to end systole. However, the bullseye plots for the patient suffering from heart failure showed no considerable change in the local fractal dimension values between end diastole and end systole. This was consistent with the initial hypothesis; as the heart contracts the trabeculae get compressed resulting in a smoother structure of the endocardium at end systole. The patient suffering from heart failure had suppressed cardiac function which led to the insufficient contraction of the cardiac wall, and hence no considerable change in the structure of the trabeculae between end diastole and end systole. The relative change in the sum of the local fractal dimensions of all points on the endocardial wall between end diastole and end systole was calculated for each case. The normal cohort had a median value of 0.137 with a standard deviation of 0.058, while the value for the patient with heart failure was 0.002, ~3 standard deviations and two orders of magnitude different.

The method was tested for its sensitivity to the size of the local neighborhood. The smaller neighborhood sizes captured features of the endocardium at a finer scale, while the bigger neighborhoods gave a more global characterization of the endocardium. It was concluded that all neighborhood sizes were able to clearly differentiate between the normal and abnormal cases and the choice of the neighborhood size depended on the objective of the user of the method. Smaller neighborhoods will capture finer anatomical features and provide a more localized characterization of the endocardium and maybe useful to detect regions of ischemic cardiac tissue. Larger neighborhood sizes maybe useful to assess cardiac function on a global scale, as was seen in the patient suffering from heart failure. Another point worth mentioning is that the computational time increases as the size of the neighborhood is increased. A neighborhood size of 4 is faster than a neighborhood size of 128 by more than two orders of magnitude. Lastly, though the neighborhood size of 4 was able to differentiate between the normal and abnormal cases, it did not provide a consistent characterization of the endocardium and seemed more like a random distribution of fractal dimension values. Also, at the length scale of 4, it is unclear if the method is still measuring the fractal dimension of the endocardium or is it just a crude measure of roughness. This result highlights the fact that maybe a simpler parameter measuring the surface roughness of the endocardium would be sufficient to capture the mechanics of left ventricular contraction.

The sensitivity of the method to the observer inputted initial threshold value was analyzed. It was determined that there is a finite window of threshold values which represents the ventricle in its true anatomical form. Values greater or lower than this range will result in an under-represented or over-represented left ventricle respectively. The study was performed on 11 different threshold values within this finite window of values for each of the 11 patients. For a range of threshold values within this window, it was observed that the fractal dimension of the endocardium at end diastole changes less than 1%. It was concluded that the method was not significantly sensitive to threshold values chosen within this range. The next part of the study aimed at assessing the likelihood of the observer to select a threshold value within this range. Three observers, with no formal training in the field, recorded their choice of the initial threshold for all 11 patients independently. All values chosen by the observers lay in the range of threshold values defining less than a 1% change between successive values of the fractal dimension.

The method met the initial objectives laid out. It is non-invasive, quick, simple to use with minimal operator involvement, and can minimize patient exposure to ionizing radiations as it requires the heart to be imaged only at end diastole and end systole. However, the method may not be suited for identifying regions of unhealthy cardiac tissue on the septal side of the left ventricle. The septum is relatively smooth and does not have a great degree of trabeculation, and is therefore difficult to capture the change in structural complexity between end diastole and end systole.

Future work on the method would be to test it on more number of abnormal cases. The statistics performed in this thesis are very rudimentary due to a single abnormal test case being available at the time. The method could also be validated with other existing quantitative techniques to draw a comparison on its performance.